



**HAL**  
open science

## Composition of inner main-belt planetesimals

J. Bourdelle de Micas, Sonia Fornasier, C. Avdellidou, Marco Delbo, Gerard T. van Belle, P. Ochner, Will M. Grundy, Nicholas A. Moskovitz

► **To cite this version:**

J. Bourdelle de Micas, Sonia Fornasier, C. Avdellidou, Marco Delbo, Gerard T. van Belle, et al..  
Composition of inner main-belt planetesimals. *Astronomy and Astrophysics - A&A*, 2022, 665, pp.A83.  
10.1051/0004-6361/202244099 . hal-03803921

**HAL Id: hal-03803921**

**<https://hal.science/hal-03803921>**

Submitted on 7 Oct 2022

**HAL** is a multi-disciplinary open access archive for the deposit and dissemination of scientific research documents, whether they are published or not. The documents may come from teaching and research institutions in France or abroad, or from public or private research centers.

L'archive ouverte pluridisciplinaire **HAL**, est destinée au dépôt et à la diffusion de documents scientifiques de niveau recherche, publiés ou non, émanant des établissements d'enseignement et de recherche français ou étrangers, des laboratoires publics ou privés.



Distributed under a Creative Commons Attribution 4.0 International License

# Composition of inner main-belt planetesimals

J. Bourdelle de Micas<sup>1</sup>, S. Fornasier<sup>1,2</sup>, C. Avdellidou<sup>3</sup>, M. Delbo<sup>3</sup>, G. van Belle<sup>4</sup>, P. Ochner<sup>5,6</sup>,  
W. Grundy<sup>4</sup>, and N. Moskovitz<sup>4</sup>

<sup>1</sup> LESIA, Observatoire de Paris, Université PSL, CNRS, Sorbonne Université, Université Paris Cité, 5 place Jules Janssen, 92195 Meudon, France

e-mail: [jules.bourdelledemicas@obspm.fr](mailto:jules.bourdelledemicas@obspm.fr)

<sup>2</sup> Institut Universitaire de France (IUF), 1 rue Descartes, 75231 Paris Cedex 05, France

<sup>3</sup> Université Côte d'Azur, CNRS-Lagrange, Observatoire de la Côte d'Azur, CS 34229, 06304 Nice Cedex 4, France

<sup>4</sup> Lowell Observatory, 1400 West Mars Hill Road, Flagstaff, AZ 86001, USA

<sup>5</sup> INAF Osservatorio Astronomico di Padova, Vicolo dell'Osservatorio 5, 35122 Padova, Italy

<sup>6</sup> Dipartimento di Fisica e Astronomia G. Galilei, Università di Padova, Vicolo dell'Osservatorio 3, 35122 Padova, Italy

Received 24 May 2022 / Accepted 1 July 2022

## ABSTRACT

**Aims.** We carried out a spectroscopic survey in order to investigate the composition of 64 asteroids of the inner main belt, which are leftovers of the original planetesimals of our Solar System (we call them inner main belt planetesimals or IMBPs). Following published methods, we identified IMBPs in the inverse size ( $1/D$ ) versus semimajor axis ( $a$ ) space, after the removal of all asteroids belonging to collisional families.

**Methods.** We conducted several ground-based observational campaigns of these IMBPs in the visible range at the 1.82 m Asiago telescope, and in the near-infrared range at the Telescopio Nazionale *Galileo*, the Lowell Discovery Telescope, and the NASA InfraRed Telescope Facility telescopes. As several of the identified planetesimals already have spectra published in the literature, we collected all the available data and focused the telescope time to investigate those never observed before, or to complete the 0.45–2.5  $\mu\text{m}$  range spectrum for those for which there is only partial spectral coverage or data with poor signal-to-noise ratio. In this way, we obtained new spectra for 24 IMBPs. Combining new and literature observations, we present spectra for 60 IMBPs in both the visible and near-infrared range, and 4 IMBPs in the visible only. All spectra were classified following well-established taxonomies. We also characterized their spectral absorption bands – when present –, their spectral slopes, and their mineralogy. In addition, we performed curve matching between astronomical and laboratory spectra in order to identify the closest meteorite analog using the RELAB database.

**Results.** The majority of the IMBPs belong to the S-complex; the latter are best matched with ordinary chondrite meteorites, and their olivine/(olivine and pyroxene) abundance ratio is not correlated with the semi-major axis. This result does not support the hypothesis that this ratio increases with heliocentric distance. Furthermore, ~27% of the IMBPs belong to the C-complex, where Ch/Cgh types dominate, meaning that most of the carbonaceous-rich planetesimals were aqueously altered. These are best fitted by CM2 carbonaceous chondrite meteorites. Finally, the remaining IMBPs (~20%) belong to the X-complex, and have various mineralogies and meteorite matches, while a few are end-member classes, including L-, K-, V-, and D- or T-types.

**Conclusions.** Our spectroscopic investigation of IMBPs confirms that silicate-rich bodies dominated the inner main belt where temperature has permitted the condensation of silicate rocks. However, almost all the spectral types are found, with the notable exception of olivine-rich A-types and Q-type asteroids. Their absence, as well as the absence of the R- and O-types among planetesimals, might be due to the rarity of these types among large asteroids. However, the absence of Q-types among primordial planetesimals is expected, as they have undergone surface rejuvenating processes. Therefore, Q-types have relatively young and less weathered surfaces compared to other types. Our results support the hypothesis of compositional mixing in the early Solar System. In particular, the fact that most of the C-complex planetesimals are aqueous altered, and the presence of three D- or T-type asteroids among them indicate that these bodies migrated from beyond 3 au to their current position.

**Key words.** minor planets, asteroids: general – techniques: spectroscopic – methods: observational

## 1. Introduction

The small bodies of the Solar System are remnants of the building blocks from which the terrestrial planets and the core of the giant planets accreted 4.5 Gyr ago. As such, they are considered our best tracers for the processes that occurred during the earliest history of the Solar System. In particular, the compositional gradient in the asteroid population is crucial for constraining models of the formation of our Solar System (Gradie & Tedesco 1982; DeMeo et al. 2014, 2009; Levison et al. 2009; Walsh et al. 2011). So far, the compositional gradient has been derived considering all asteroids that can be reached with physical characterization methods such as radiometry, spectroscopy,

and spectrophotometry. Namely, these studies have been carried out, in general, without distinguishing the origin of asteroids (DeMeo et al. 2014). However, the current asteroid population is not dominated by planetesimals, the first large bodies (~100 km in diameter) that accreted 4.56 Gyr ago by the gravitational collapse of dust particles in the protoplanetary disk of our Sun (Cuzzi et al. 2008; Johansen 2015; Klahr & Schreiber 2020; Gerbig et al. 2020). Indeed, there is growing evidence that several of these planetesimals were broken by impacts during the collisional evolution of our Solar System, forming families of asteroid collisional fragments. These collisional fragments likely outnumber the planetesimals that survived intact for 4.5 Gyr (Delbo et al. 2017, 2019; Dermott et al. 2018).

Therefore, only a small fraction of the asteroid population includes the original leftover planetesimals (Delbo et al. 2017, 2019). These planetesimal leftovers are the oldest ones, but did not necessarily accrete where they are located today. Some of them may have been implanted in their current position during the phase of planetary migration (e.g., Walsh et al. 2011; Raymond & Izidoro 2017b). Additionally, planetary embryos that formed elsewhere and were broken by collisions, might have been implanted in the asteroid main belt before the gas dissipation phase of the Solar System (Asphaug et al. 2006; Scott et al. 2015).

In this paper, we aim to characterize the composition of the inner main-belt asteroids that are likely the survivors from primordial time and thus represent the original planetesimals. Identifying such bodies is a challenge, because it is necessary first to identify all the collisional family members, and then to remove them from the population of asteroids of the inner main belt. Classical family identification methods are highly efficient at discovering young and relatively old families, but are typically biased against the detection of very old ones ( $> 4$  Gyr), where family members are spread out from the original location due to nongravitational thermal forces (Bottke et al. 2005). Walsh et al. (2013), Bolin et al. (2017), Delbo et al. (2017), and Deienno et al. (2021) developed a new method to identify old families by searching for correlation of asteroids in the inverse of their diameter ( $1/D$ ) and proper semimajor axis ( $a$ ) space, where family members form the so-called V-shapes. In particular, family members disperse over time. A nongravitational effect called the Yarkovsky effect (Vokrouhlický et al. 2006) slowly changes the orbital semimajor axis  $a$  of asteroids at a rate of  $da/dt$  proportional to  $1/D$ . Prograde rotating asteroids have  $da/dt > 0$  and move away from the Sun, while retrograde ones with  $da/dt < 0$  move towards the sun. This creates correlations of points in the  $1/D$  versus  $a$  plane, which resemble the letter “V”, whose slope ( $K$ ) indicates family age (Vokrouhlický et al. 2006; Spoto et al. 2015). By removing all asteroids that are inside the V-shapes of families from the population of the inner main belt and also adding the parent bodies of some of these families, which were once planetesimals themselves, we identified 64 asteroids that are the direct leftovers of the planetesimal population (we refer to these specific objects as inner main-belt planetesimals IMBPs, hereafter).

We carried out spectroscopic surveys in the visible and near-infrared range to constrain the composition, taxonomy, and mineralogy of these IMBPs. Spectroscopy is essential, not only to characterize the composition of IMBPs but also to disentangle planetesimals from asteroids, that is, members of a given family, especially for bodies close to the V-shape borders where the dynamical distinction may be difficult. In Sect. 2, we explain the method that we used to distinguish planetesimals among the inner main-belt asteroid population, and in Sect. 3, we explain the observing strategy, the data reduction procedures, and the different spectral analysis applied for this study. Section 4 is dedicated to the taxonomical and mineralogical characterization of the IMBPs, while in Sect. 5, we provide the implications of our findings concerning the compositional gradient and migration theories of the early Solar System.

## 2. Selection of planetesimals

We follow the approach of Delbo et al. (2017) in order to identify asteroids of the inner main belt that could be planetesimals. These authors showed that the inner main belt contains asteroids

**Table 1.** Properties of the asteroid families in terms of center  $a_c$  and slope  $K$  of their V-shapes.

Name	$a_c$ (au)	$K$ (au <sup>-1</sup> km <sup>-1</sup> )	Reference
Low albedo			
Klio	2.362	2.65	1
Primordial <sup>L</sup>	2.367	0.59	2
Erigone	2.376	9.22	1
Chaldea	2.376	1.99	1
Primordial <sup>R</sup>	2.400	0.59	2
Clarissa	2.406	33.65	1
Polana	2.420	1.10	2
Chimaera	2.460	6.14	1
Sulamitis	2.463	5.02	1
Svea	2.476	6.14	1
Eulalia	2.490	1.70	2
High albedo			
Flora	2.200	1.60	2
Baptistina	2.260	11.90	3
Euterpe	2.347	7.67	1
Primordial	2.363	0.68	4
Vesta	2.370	2.97	1
Athor	2.380	1.72	3
Massalia	2.400	14.12	1
Hertha1	2.412	8.36	5
Hertha2	2.426	31.35	5

**Notes.** For the low-albedo primordial family of Delbo et al. (2017), we give the inward (left) and outward (right) borders. The former is indicated with the <sup>L</sup>, while the latter with the <sup>R</sup> as a suffix to the family name.

**References.** (1) Nesvorný et al. (2015), (2) Delbo et al. (2017), (3) Delbo et al. (2019), (4) Delbo et al. (in prep.), and (5) Dykhuis & Greenberg (2015).

of two different origins: (i) those that are collisional fragments of other asteroids that formed in the current location and are, in general, inside the V-shapes of asteroid collisional families, and (ii) those that are outside those V-shapes. This latter population therefore contains asteroids that were not created as collisional fragments in the main belt and are likely planetesimals that accreted directly from the protoplanetary disk. In this work, we also include in the planetesimal list the parent bodies of the known collisional families. This is because these objects, in general, could have also formed as planetesimals before they broke up. We also identified some cases where relatively large asteroids reside inside family V-shapes; however, their spectral class is clearly distinct from that of the overlapping family, and therefore we also included these asteroids in our planetesimal list.

Firstly, we separated the low-albedo from the moderate- and high-albedo asteroid populations, using 0.12 as the geometric visible albedo ( $p_V$ ) threshold between the two populations, following a previous approach (Delbo et al. 2017). Next, for each albedo population, we drew the V-shapes associated to all known families of the inner main belt (from Walsh et al. 2013; Dykhuis & Greenberg 2015; Nesvorný et al. 2015; Delbo et al. 2017, 2019, as shown in Table 1) and identified those asteroids that lie outside those V-shapes (Fig. 1).

For this work, we split the Nysa-Polana dynamical complex – which is listed as a single entry in Table 2 of

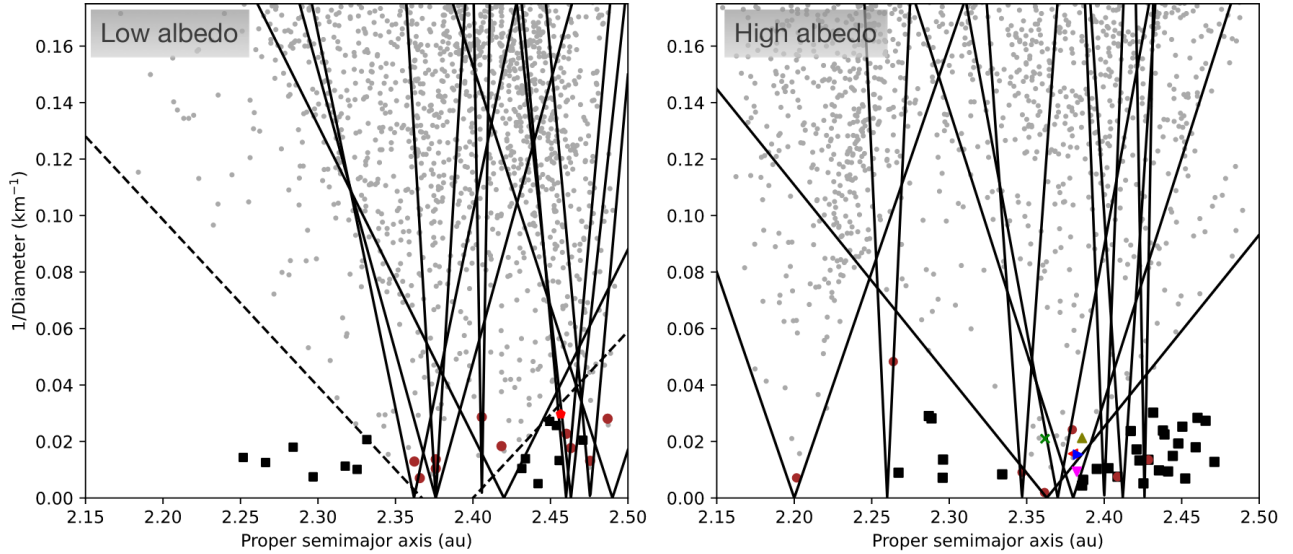


**Fig. 1.** Inverse diameter vs. proper semi-major axis for the populations of inner main-belt asteroids (gray circles) with  $p_V \leq 0.12$  (right panel) and with  $p_V > 0.12$  (left panel). The black solid squares represent objects that are outside the V-shapes of known families and are therefore included in our list of planetesimals. The solid red circles are the parent bodies (or largest members) of known families, which we also include in the list of planetesimals. Asteroids that are clearly compositionally distinct from the V-shape family in which they reside are marked with filled symbols, namely a red pentagon for (732) Tjilaki, a red left-pointing triangle for (172) Baucis, a green cross for (186) Celuta, a magenta upside-down triangle for (230) Athamantis, an olive triangle for (234) Barbara, and a blue right-pointing triangle for (337) Devosa. See text for the method used for the selection. The primordial family of low-albedo asteroids is represented inside the V-shape delimited by the two dashed lines, as described by Delbo et al. (2017).

Nesvorný et al. (2015) but is known to contain several collisional families – into the low-albedo Eulalia and Polana families (Walsh et al. 2013) and the high-albedo Hertha1 and Hertha2 families (Dykhuis & Greenberg 2015). Apart from the families listed in Table 1, Nesvorný et al. (2015) reports three more small families, (1270) Datura, (1892) Lucienne, and (21509) Lucascavin. However, the potential parents of the Datura and Lucascavin families are also reported as members of the nearby Flora or Baptistina families. The parameters of the V-shapes of Datura and Lucascavin families are not known. However, given the small number of the members of these families and their compactness in orbital element space, their V-shapes are extremely narrow and mostly contained within those of Flora or Baptistina. These small families could, alternatively, be second-generation families formed from the breakup of a member of the Flora or Baptistina families, and therefore we do not consider their parent bodies as planetesimals in this work. The Lucienne family is compact and therefore has a very narrow V-shape, which does not affect the selection of the potential planetesimal population. Given the small size ( $\sim 10$  km) of its parent body and that all family members overlap with the V-shape of another family, it is likely the Lucienne family is the result of a second-generation fragmentation (the parent body was already a fragment of another family). Thus, we do not select the Lucienne family parent as a planetesimal.

Finally, another very small and compact family whose parent is the asteroid (108138) 2001 GB<sub>11</sub>, is reported by Nesvorný et al. (2015). The corresponding V-shape, for which no parameters are reported in the literature, is very narrow and does not affect the selection of planetesimals. In addition, because of the lack of physical properties for the family members, such as spectra, diameters, and albedo, we choose not to include the parent body of this family as a potential planetesimal. The family of (689) Zita is also not included because of the fact that its detection has low statistical significance, and it is debatable whether Zita itself is the real family parent (Delbo et al. 2019). Furthermore,

its V-shape does not affect the selection process for this work.

A V-shape in the plane of the proper semimajor axis ( $a$ ) and inverse diameter ( $1/D$ ) is characterized by the  $a$ -value of its vertex ( $a_c$ ) and slope of the sides  $K$  (e.g., Bolin et al. 2017, where small and large values of  $K$  indicate old and young families, respectively). The V-shape parameters  $a_c$  and  $K$  adopted for this work and given in Table 1 were taken directly from the work of Delbo et al. (2017, 2019). However, for most of the families, an equivalent representation of the V-shape in the  $a$  and absolute magnitude ( $H$ ) plane is used in the literature. In this case, the slope of the V-shape is expressed in terms of the so-called  $C$  parameter (Vokrouhlický et al. 2006), which is related to the  $K$ -value by Eq. (1):

$$K = \frac{\sqrt{p_V}}{1329 C}. \quad (1)$$

Hence, we used the literature  $C$ - and  $p_V$ -values in Eq. (1) to calculate the corresponding  $K$ -values. For the Hertha1 and Hertha2 families of Dykhuis & Greenberg (2015), we take from their work  $a_c = 2.412$  au,  $C = 0.45 \times 10^{-4}$  au,  $p_V = 0.25$  and  $a_c = 2.426$  au,  $C = 0.12 \times 10^{-4}$  au,  $p_V = 0.25$ , respectively. The other  $C$ - and  $p_V$ -values are taken from Table 2 of Nesvorný et al. (2015), where the  $a_c$  is not reported. We therefore assume that  $a_c$  coincides with the proper semimajor axis of each family parent body.

We defined an asteroid as lying inside a V-shape if  $1/D > -K(a - a_c)$  and  $1/D > K'(a - a'_c)$ , where  $D$  is the asteroid diameter,  $(K, a_c)$  and  $(K', a'_c)$  are the V-shape parameters for the inward (or left) side and outward (or right) side of the V-shape, respectively. When the inward and the outward sides have the same vertex and slope, only the nonprimed version of the parameters is used.

After having identified the family V-shapes of the inner main belt, as shown in Fig. 1, we found 29 high-albedo and

14 low-albedo asteroids that clearly lie outside any family V-shape. In addition to the asteroids that lie outside the V-shapes, we also add to the planetesimal list the largest fragments of the collisional families of Table 1. It is natural to do so, as these families were produced by the in situ fragmentation of parent bodies, which were likely planetesimals themselves. These are seven high-albedo and ten low-albedo asteroids. The latter situation is possible, in particular in the cases of the very narrow V-shapes, because of the asymmetric initial ejection of the family fragments.

Moreover, we noted that (337) Devosa, (172) Baucis, and (234) Barbara, which are spectroscopically classified in the literature as Xk, L, and L, respectively, are in a location of the overlapping V-shapes of the Athor family (Delbo et al. 2019), which is spectroscopically distinct as it is composed of Xc-type asteroids, and of a primordial, high-albedo family that mostly consists of S-complex members (Delbo et al., in prep.). Because these three asteroids have a different composition from the Athor and the primordial S-complex family, we include them in our list of planetesimals. In addition, the asteroid (230) Athamantis overlaps with the V-shape of the Athor family, but it is clearly distinct from this family because Athamantis belongs to the S-complex, and thus we also add it to our list of potential planetesimals. Furthermore, (186) Celuta, which is classified as K-type, overlaps with the V-shape of the aforementioned primordial, high-albedo family that mostly consists of S-complex members (Delbo et al., 2022). Because of this classification mismatch, it is unlikely that Celuta is a fragment from the parent body of the primordial and high-albedo family, and therefore we add it to the list of the planetesimals. Finally, (732) Tjilaki, which is classified as a D-type, overlaps with the V-shapes of the Chimaera and Sulamitis families, whose members belong to the C-complex (Morate et al. 2018, 2019; Arredondo et al. 2021). However, the proper inclination and eccentricity of Tjilaki are very different from those of the compact Chimaera and Sulamitis families. For both these compositional and dynamical arguments, we include (732) Tjilaki in our planetesimal list.

Potential biases in the list of asteroids that we identify here as planetesimals arise for uncertainties in the determination of the V-shape slopes and vertexes of the known families. These could potentially affect the selection, in particular among the low-albedo population of asteroids with a  $<2.35$  au: uncertainties in the slope of the 4 Gyr-old V-shape of Delbo et al. (2017) could determine the inclusion or the exclusion of the asteroids (261) Prynno, (370) Modestia, (442) Eichsfeldia, and (853) Nansenia in the list of planetesimals. However, this would not dramatically affect our results, because two of these asteroids are Ch-type and two are X-type. It is also interesting to note that, apart from the asteroids mentioned above, the list of planetesimals is robust against the method that removes collisionally produced asteroids. In particular, Delbo et al. (in prep.) showed that the size frequency distribution of the planetesimals does not substantially change depending on whether family members are removed using the family list of Nesvorný et al. (2015) or using the V-shape identification performed here. The bulk of the planetesimals identified here have diameters  $D$  of greater than 35 km, as also found by Delbo et al. (2017). Most of the  $D > 35$  km asteroids in the inner main belt have taxonomic classification from this work or the literature on the basis of spectroscopy or spectrophotometry. It is therefore unlikely that some planetesimals have been added to families as interlopers because of the lack of taxonomic classification.

The list of all IMBPs is shown in Tables 2 and 3.

### 3. Data acquisition and reduction

In order to study the composition of the total IMBP population and to optimize the observing time at telescopes, we first inspected asteroid spectroscopy databases and individual papers to obtain the existing data. Being relatively bright, 56 out of 64 of the IMBPs were already observed in the visible (VIS) and/or in the near-infrared (NIR) range. Specifically, we collected 28, 24, and 21 spectra in the VIS, NIR, and VIS-NIR wavelength ranges, respectively. We then focused our new observations on IMBPs that had never been observed before or for which the data have a low signal-to-noise ratio or are missing the VIS-NIR range.

#### 3.1. Visible observations

We obtained a total of 14 new spectra in the VIS range. Eight of these were acquired at the 1.82 m *Copernico* Telescopio located at Cima Ekar, Asiago, Italy. We used the Asiago Faint Spectroscopic Camera (AFOSC, Tomasella et al. 2016) equipped with a low-resolution Volume Phase Holographic (VPH#6) grism, and a 4.2'' slit, covering the 0.52–0.95  $\mu\text{m}$  range. Five other spectra were obtained at the 1.20 m Asiago telescope using a Boller and Chivens spectrograph with two different resolution gratings (150 and 300  $\text{gr mm}^{-1}$ ) and a wide slit of 4.2''. With this setup, we covered the  $\sim 0.40$ – $0.85$   $\mu\text{m}$  wavelength range with a dispersion of 340  $\text{\AA mm}^{-1}$ . Finally, we also included an unpublished observation of (234) Barbara in our dataset, which was acquired in 2007 at the 3.6 m New Technology Telescope (NTT) based at La Silla. We used the ESO Multi-Mode Instrument (EMMI) with the low-resolution grism #1 (150  $\text{gr mm}^{-1}$ ) in RILD mode, and a 2'' slit, covering the 0.45–0.95  $\mu\text{m}$  range. The observing strategy is the same as that presented by Fornasier et al. (2008, 2010). During each observing night, several solar analog stars (here after SA stars) were observed for the removal of the solar contribution from the asteroid spectra. Standard calibration including bias, flat-field, and wavelength calibration lamps were obtained during the daytime before the observations.

#### 3.2. Near-infrared observations

In the NIR range, we observed a total of 16 IMBP using three different telescopes between 2017 and 2022. The majority of the spectra (12) were obtained from a dedicated observing program carried out at the 3.58 m Telescopio Nazionale *Galileo* (TNG) based at la Palma, Spain. The spectrometer used was the Near-Infrared Camera Spectrometer (NICS; Baffa et al. 2001) equipped with the Amici prism and a 2.0'' slit, covering the 0.8–2.5  $\mu\text{m}$  wavelength range with a spectral resolution of about 35. Two asteroids were observed with the 3.2 m NASA InfraRed Telescope Facility (IRTF) based at Mauna Kea, USA, using the SpeX spectrograph (Rayner et al. 2003) equipped with a 0.8'' slit and a low-resolution grating, which covers the 0.85–2.40  $\mu\text{m}$  wavelength range.

Finally, three asteroids were observed with the 4.2 m Lowell Discovery Telescope (LDT) located in Flagstaff, USA. This telescope was equipped with the Near Infrared High-Throughput Spectrograph (NIHTS; Gustafsson et al. 2021) with a 1.34'' slit and a 1024×1024 pixel CCD detector with a pixel scale of 0.13''  $\text{px}^{-1}$  covering the 0.86–2.40  $\mu\text{m}$  wavelength range.

The observing strategy was one that is commonly used for NIR spectroscopy and follows the so-called ABBA procedure.

**Table 2.** Observational conditions for the IMBP.

Object	Date	UT	Exp (s)	$m_v$	$\alpha$ (°)	Airm.	SA	SA Airm.	Instrument	Slit (")
(12) Victoria	25/08/00	04:26	1500	10.9	27.6	1.14	HD 159222	1.06	B–C	4.00
(21) Lutetia	24/08/00	03:15	1200	10.3	18.3	1.47	HD 159222	1.16	B–C	4.00
(42) Isis	02/10/21	01:57	300	12.1	23.9	1.27	SA115-271	1.21	Afosc	4.22
(42) Isis	13/10/21	02:03	8 × 10	11.9	22.2	1.45	SA112-1333	1.16	NICS	2.00
(72) Feronia	23/12/19	18:46	600	13.2	25.3	1.33	Hyades 64	1.17	Afosc	4.22
(72) Feronia	06/02/20	02:56	4 × 90	13.9	24.1	1.45	SA93-101	1.39	NIHTS	1.34
(80) Sappho	23/08/00	23:01	1200	10.8	22.5	1.67	HD 159222	1.16	B–C	4.00
(83) Beatrice	06/02/20	05:45	4 × 30	11.7	5.2	1.07	HD 79930	1.14	NIHTS	1.34
(126) Velleda	13/10/21	03:58	8 × 50	13.8	24.4	1.21	BD+421949	1.33	NICS	2.00
(131) Vala	21/12/19	01:45	600	13.7	12.6	1.09	Hyades 64	1.22	Afosc	4.22
(172) Baucis	06/02/20	07:14	4 × 60	12.1	1.8	1.04	HD 79930	1.21	NIHTS	1.34
(178) Belisana	12/02/22	02:33	8 × 60	13.4	17.9	1.35	BD+112407	1.10	NICS	2.00
(186) Celuta	02/10/21	01:40	600	13.2	24.5	1.11	SA102-1081	1.61	Afosc	4.22
(189) Phthia	12/02/22	01:50	8 × 30	12.7	5.6	1.11	BD+032345	1.12	NICS	2.00
(198) Ampella	24/12/19	02:23	480	12.4	11.1	1.22	HD 89010	1.09	Afosc	4.22
(207) Hedda	13/10/21	04:45	8 × 70	14.6	25.1	1.09	SA112-1333	1.16	NICS	2.00
(234) Barbara	20/01/07	07:58	180	13.4	25.3	1.27	SA102-1081	1.21	EMMI	2.00
(248) Lameia	24/12/19	02:53	720	14.3	11.7	1.21	Hyades 64	1.21	Afosc	4.22
(326) Tamara	13/10/21	05:07	8 × 90	14.8	20.7	1.35	BD+421949	1.33	NICS	2.00
(336) Lacadiera	13/10/21	02:42	8 × 60	14.3	22.8	1.32	BD+421949	1.33	NICS	2.00
(336) Lacadiera	06/01/22	21:27	2 × 1200	13.4	11.0	1.13	Hyades 64	1.14	B–C	3.50
(376) Geometria	12/10/21	20:34	8 × 20	12.8	12.6	1.34	SA115-271	1.28	NICS	2.00
(435) Ella	02/10/17	10:38	2 × 30	12.8	8.4	1.03	SA112-1333	1.09	SpeX	0.80
(435) Ella	02/10/21	00:50	600	14.5	21.6	1.18	SA115-271	1.21	Afosc	4.22
(623) Chimaera	04/10/17	08:02	120	14.2	12.6	1.02	SA113-276	1.24	SpeX	0.80
(623) Chimaera	12/10/21	20:57	8 × 50	14.0	10.6	1.21	SA115-271	1.28	NICS	2.00
(654) Zelinda	12/10/21	21:15	8 × 30	13.3	17.9	1.06	SA112-1333	1.16	NICS	2.00
(732) Tjilaki	01/10/21	22:41	900	13.7	2.0	1.48	SA115-271	1.21	Afosc	4.22
(732) Tjilaki	12/10/21	22:51	8 × 50	14.0	6.7	1.23	SA115-271	1.28	NICS	2.00
(914) Palisana	24/08/00	23:31	1200	11.7	22.3	1.08	HD 191854	1.00	B–C	4.00
(914) Palisana	12/02/22	01:12	8 × 60	13.8	13.3	1.83	HD 89474	1.74	NICS	2.00

**Notes.** Here, we present the number and name of the asteroids, observation date and time at the beginning of the acquisition, exposure time, visual magnitude ( $m_v$ ), phase angle ( $\alpha$ ), airmass at the middle of the exposure time, solar-analog star used for reduction (see Sect. 3.3) with the associated airmass, instrument and slit used. B–C stands for Boller and Chivens spectrograph.

The target is observed at two different positions (named A and B) in the slit with a relatively short individual integration time (of the order of 2 min or less depending on the magnitude of the targets) during which the atmosphere may be considered stable. These pairs of observations are subtracted, allowing the removal of sky background, and pairs of observations are repeated until the desired S/N is reached.

During each night, we observed several stars close in time and in airmass to the asteroids. We observed G2V-type trusted SAs in order to remove the solar contribution, and to correct the telluric features. In several cases, we also observed G and F spectral type stars in proximity to our targets in order to perform a better telluric correction of the spectrum. Additionally, flat-fields and lamp spectra were also acquired for wavelength calibration during each run. However, for the TNG wavelength calibration, the low resolution of the NICS-Amici prism setup impeded the correct identification of Ar/Xe lamps lines, which are blended. For these observations, the wavelength calibration was done using a table providing the theoretical dispersion of the instrument, made available by the TNG team. Adjustments of the wavelength calibration were later applied, when needed, using some well-known atmospheric features.

### 3.3. Data reduction

SpeX and NIHTS spectra were reduced with the Spextool (Spectral EXtraction Tool; Cushing et al. 2004), which is an IDL package. The remaining observations were reduced using the ESO-Midas package (Banse et al. 1983). We applied standard reduction procedures as described by Fornasier et al. (1999, 2010), which include subtraction of the bias from the raw data, flat-field correction, cosmic-ray removal, background subtraction, reducing the two-dimensional spectra to one-dimension, wavelength calibration and, for the visible spectra, atmospheric extinction correction. This last correction was done using the asteroid airmass at the time of a given observation and the Asiago atmospheric extinction coefficients provided in the 3000–10 000 Å wavelength range by the *Copernico* Telescope team<sup>1</sup>.

For the NIR spectra, the background was removed, producing A–B and B–A pair frames, and the final spectra were obtained by shifting and adding all the positive spectra of the A–B and

<sup>1</sup> <https://www.oapd.inaf.it/sede-di-asiago/telescopes-and-instrumentations/copernico-182cm-telescope/afosc>

**Table 3.** Full list of the IMBP used in this work.

Objects	$D$ (km)	$p_V$	$a$ (au)	Tax.	$S_{\text{all}}$ (%/10 <sup>3</sup> Å)	$S_{\text{vis}}$ (%/10 <sup>3</sup> Å)	$S_{\text{NIR1}}$ (%/10 <sup>3</sup> Å)	$S_{\text{NIR2}}$ (%/10 <sup>3</sup> Å)	Ref
(4) Vesta	519.3	0.347 ± 0.010	2.362	V	0.76 ± 0.10	5.90 ± 0.09	2.15 ± 0.20	3.34 ± 0.33	3
(6) Hebe	193.7	0.258 ± 0.007	2.425	S	1.55 ± 0.07	10.67 ± 0.16	2.80 ± 0.11	0.47 ± 0.08	3
(7) Iris	228.3	0.234 ± 0.014	2.386	S	1.60 ± 0.06	11.32 ± 0.11	3.82 ± 0.07	0.59 ± 0.07	3
(8) Flora	140.7	0.256 ± 0.007	2.202	S	3.39 ± 0.17	15.23 ± 0.38	7.19 ± 0.16	1.32 ± 0.22	10,20
(9) Metis	155.7	0.160 ± 0.008	2.386	S	1.81 ± 0.03	6.34 ± 0.04	3.71 ± 0.05	0.86 ± 0.04	3,9
(11) Parthenope	145.1	0.196 ± 0.005	2.452	Sq	2.11 ± 0.04	8.33 ± 0.12	4.29 ± 0.06	1.53 ± 0.05	3
(12) Victoria	119.6	0.159 ± 0.006	2.334	Sq	5.34 ± 0.06	10.17 ± 0.07	9.31 ± 0.30	1.72 ± 0.28	1
(17) Thetis	78.3	0.175 ± 0.006	2.471	S	2.75 ± 0.09	13.04 ± 0.14	3.93 ± 0.12	1.01 ± 0.11	3
(18) Melpomene	139.6	0.233 ± 0.007	2.296	S	3.29 ± 0.11	11.23 ± 0.53	4.65 ± 0.25	1.26 ± 0.34	2,5
(19) Fortuna	196.7	0.053 ± 0.005	2.442	Ch	1.79 ± 0.02	-1.18 ± 0.06	2.75 ± 0.04	1.11 ± 0.05	16,3
(20) Massalia	132.9	0.214 ± 0.010	2.409	S	2.21 ± 0.06	9.60 ± 0.09	3.69 ± 0.10	1.53 ± 0.11	3
(21) Lutetia	102.1	0.223 ± 0.010	2.435	Xc	0.95 ± 0.04	5.63 ± 0.09	0.52 ± 0.03	-0.37 ± 0.02	1,3
(27) Euterpe	110.3	0.223 ± 0.023	2.347	S	2.38 ± 0.08	13.03 ± 0.14	5.97 ± 0.11	0.69 ± 0.09	3
(40) Harmonia	111.8	0.210 ± 0.011	2.267	S	1.32 ± 0.06	11.44 ± 0.10	2.34 ± 0.07	0.30 ± 0.11	3
(42) Isis	106.4	0.160 ± 0.006	2.441	Sq	5.47 ± 0.06	8.86 ± 0.05	10.75 ± 0.55	-0.72 ± 0.45	1
(44) Nysa	75.4	0.505 ± 0.019	2.423	Xk	1.62 ± 0.02	3.18 ± 0.03	1.18 ± 0.05	0.72 ± 0.05	17
(51) Nemausa	142.2	0.087 ± 0.002	2.366	Cgh	2.12 ± 0.03	1.00 ± 0.09	3.23 ± 0.09	-0.06 ± 0.07	16,20
(63) Ausonia	97.2	0.158 ± 0.006	2.395	S	2.65 ± 0.09	16.74 ± 0.17	5.12 ± 0.12	1.35 ± 0.11	3
(67) Asia	58.1	0.239 ± 0.009	2.421	S	1.51 ± 0.06	11.68 ± 0.14	3.43 ± 0.08	1.15 ± 0.10	3
(72) Feronia	79.6	0.072 ± 0.003	2.266	D	10.53 ± 0.06	14.30 ± 0.04	9.93 ± 0.27	1.51 ± 0.65	1
(79) Eurynome	67.2	0.269 ± 0.008	2.444	S	1.78 ± 0.05	9.69 ± 0.10	3.31 ± 0.13	1.11 ± 0.08	3
(80) Sappho	73.6	0.180 ± 0.004	2.296	S	4.37 ± 0.15	17.58 ± 0.12	6.22 ± 0.25	1.29 ± 0.25	1,5
(83) Beatrix	96.0	0.078 ± 0.003	2.432	Xk	3.25 ± 0.02	3.99 ± 0.08	3.91 ± 0.06	1.54 ± 0.05	1,5
(84) Kilo	77.5	0.054 ± 0.002	2.362	Xc	1.04 ± 0.01	2.84 ± 0.03	0.90 ± 0.05	0.03 ± 0.002	14,9
(112) Iphigenia	71.9	0.039 ± 0.002	2.434	Cgh	1.74 ± 0.03	1.88 ± 0.04	0.74 ± 0.08	0.17 ± 0.08	4,12
(118) Peitho	41.9	0.210 ± 0.009	2.438	S	1.93 ± 0.08	12.01 ± 0.10	3.17 ± 0.16	0.67 ± 0.10	3
(126) Velleda	44.5	0.160 ± 0.006	2.439	S	4.10 ± 0.07	11.37 ± 0.05	6.88 ± 0.53	-0.19 ± 0.61	1
(131) Vala	33.1	0.142 ± 0.001	2.432	K	1.53 ± 0.02	5.35 ± 0.05	2.91 ± 0.07	1.18 ± 0.05	1,20
(135) Hertha	74.0	0.155 ± 0.005	2.429	Xk	2.07 ± 0.03	5.75 ± 0.08	1.87 ± 0.04	1.27 ± 0.03	11
(136) Austria	34.5	0.157 ± 0.000	2.287	Xc	1.50 ± 0.04	5.91 ± 0.07	0.54 ± 0.06	0.38 ± 0.04	5,6
(138) Tolosa	51.9	0.208 ± 0.012	2.448	S	2.60 ± 0.04	9.21 ± 0.11	5.87 ± 0.08	1.40 ± 0.09	9,10
(142) Polana	54.5	0.041 ± 0.002	2.419	B	0.41 ± 0.04	-2.00 ± 0.03	1.30 ± 0.04	1.08 ± 0.04	3
(161) Athor	41.4	0.191 ± 0.009	2.379	Xc	1.16 ± 0.02	3.75 ± 0.08	1.39 ± 0.05	0.13 ± 0.05	12
(163) Erigone	73.0	0.043 ± 0.002	2.366	Cgh	1.60 ± 0.04	1.60 ± 0.04	-	-	5
(172) Baucis	63.9	0.142 ± 0.004	2.380	L	2.36 ± 0.07	11.97 ± 0.16	3.99 ± 0.05	-1.54 ± 0.09	1,18
(178) Belisana	35.3	0.253 ± 0.010	2.460	S	4.10 ± 0.10	12.14 ± 0.11	8.30 ± 0.43	0.09 ± 0.33	5,1
(182) Elsa	42.2	0.208 ± 0.009	2.418	S	1.34 ± 0.07	11.74 ± 0.15	2.24 ± 0.19	1.05 ± 0.12	5,9
(186) Celuta	47.7	0.204 ± 0.009	2.362	K	2.08 ± 0.03	10.23 ± 0.11	4.16 ± 0.07	0.16 ± 0.05	1,5
(189) Phthia	39.6	0.221 ± 0.012	2.450	S	3.42 ± 0.10	15.51 ± 0.11	7.91 ± 0.49	-0.14 ± 0.23	5,1
(192) Nausikaa	94.7	0.248 ± 0.007	2.403	S	3.38 ± 0.09	15.17 ± 0.13	6.72 ± 0.13	1.35 ± 0.10	4
(198) Ampella	55.7	0.227 ± 0.013	2.459	S	1.01 ± 0.04	7.27 ± 0.05	1.32 ± 0.20	-0.62 ± 0.13	1,13
(207) Hedda	55.6	0.043 ± 0.001	2.284	Cgh	1.03 ± 0.02	0.34 ± 0.05	0.21 ± 0.15	-0.28 ± 0.21	4,1
(230) Athamantis	107.4	0.183 ± 0.005	2.382	S	13.91 ± 0.11	13.91 ± 0.11	-	-	5
(234) Barbara	47.1	0.208 ± 0.007	2.386	L	3.96 ± 0.08	14.03 ± 0.06	4.42 ± 0.08	-0.24 ± 0.12	1,3
(248) Lameia	48.9	0.068 ± 0.002	2.471	X-comp.	4.24 ± 0.05	4.24 ± 0.05	-	-	1
(261) Prymno	48.4	0.114 ± 0.004	2.332	Xk	1.99 ± 0.02	3.32 ± 0.07	2.03 ± 0.03	1.43 ± 0.04	3
(298) Baptistina	20.7	0.135 ± 0.013	2.264	S	1.27 ± 0.02	4.30 ± 0.06	3.58 ± 0.24	-0.01 ± 0.17	4,21
(302) Clarissa	34.9	0.050 ± 0.003	2.406	C	0.77 ± 0.01	1.85 ± 0.03	1.51 ± 0.08	1.12 ± 0.06	15,3
(313) Chaldaea	95.9	0.051 ± 0.001	2.375	Cgh	2.14 ± 0.02	0.17 ± 0.03	3.51 ± 0.09	-0.07 ± 0.27	14
(326) Tamara	88.9	0.038 ± 0.001	2.318	Ch	0.49 ± 0.03	-0.17 ± 0.04	0.20 ± 0.28	-1.79 ± 0.34	8,1
(329) Svea	76.0	0.040 ± 0.001	2.476	C	1.37 ± 0.01	1.61 ± 0.03	1.45 ± 0.09	1.40 ± 0.13	13,7
(336) Lacadiera	69.8	0.043 ± 0.002	2.252	T/D	3.64 ± 0.05	5.37 ± 0.09	3.60 ± 0.41	0.61 ± 0.47	1
(337) Devosa	65.1	0.127 ± 0.006	2.383	Xk	1.52 ± 0.02	2.85 ± 0.08	1.68 ± 0.05	1.26 ± 0.04	5,12
(345) Tercidina	99.0	0.057 ± 0.003	2.325	Ch	1.19 ± 0.02	-0.79 ± 0.08	2.00 ± 0.04	0.96 ± 0.04	3
(376) Geometria	35.5	0.210 ± 0.020	2.289	S	3.28 ± 0.10	14.52 ± 0.14	7.22 ± 0.40	0.79 ± 0.29	5,1
(435) Ella	36.9	0.080 ± 0.004	2.449	Xc	1.01 ± 0.01	3.03 ± 0.06	1.21 ± 0.12	1.09 ± 0.08	1
(474) Prudentia	39.4	0.052 ± 0.007	2.454	C	1.96 ± 0.07	1.96 ± 0.07	-	-	11
(495) Eulalia	35.6	0.058 ± 0.002	2.488	B	-0.68 ± 0.02	-1.10 ± 0.05	-1.06 ± 0.10	0.50 ± 0.03	10,13
(556) Phyllis	36.6	0.193 ± 0.008	2.465	S	0.63 ± 0.04	8.25 ± 0.08	0.78 ± 0.09	0.63 ± 0.09	5,13
(623) Chimaera	44.0	0.035 ± 0.001	2.460	Cgh	1.89 ± 0.02	2.66 ± 0.04	0.72 ± 0.32	2.27 ± 1.60	14,1
(654) Zelinda	133.9	0.045 ± 0.001	2.297	Ch	1.49 ± 0.02	0.47 ± 0.03	1.32 ± 0.24	-0.46 ± 0.31	7,1
(732) Tjilaki	33.7	0.067 ± 0.004	2.457	D	16.97 ± 0.05	14.74 ± 0.06	19.17 ± 0.68	12.21 ± 0.64	1
(752) Sulamitis	56.6	0.039 ± 0.002	2.463	Cgh	3.44 ± 0.03	2.12 ± 0.02	4.16 ± 0.18	1.22 ± 0.91	15,19
(914) Palisana	75.4	0.103 ± 0.002	2.456	Ch	1.96 ± 0.02	-0.30 ± 0.04	1.60 ± 0.32	0.07 ± 0.21	1

**Notes.** For each one, we report the physical parameters, the derived taxonomy, and the spectral slope values in several ranges:  $S_{\text{all}}$  for the whole spectral range;  $S_{\text{vis}}$  for the visible range, between 0.5 and 0.75  $\mu\text{m}$ ;  $S_{\text{NIR1}}$  in the 1.1–1.6  $\mu\text{m}$  range, and  $S_{\text{NIR2}}$  in the 1.7–2.2  $\mu\text{m}$  range. Ref indicates the references for where the spectra were acquired/retrieved. Albedo, diameter and semi-major axis values were taken from MP3C<sup>2</sup> database.

**References.** (1) This work, (2) Bell et al. (2005), (3) MITHNEOS IRTF survey, (4) Lazzaro et al. (2004), (5) Bus & Binzel (2002), (6) Hardersen et al. (2011), (7) Fornasier et al. (2014), (8) Vilas et al. (1993), (9) Reddy & Sanchez (2016), (10) Xu et al. (1995), (11) Fornasier et al. (2010), (12) Clark et al. (2004), (13) Fieber-Beyer et al. (2012), (14) Morate et al. (2019), (15) Morate et al. (2018), (16) Fornasier et al. (1999), (17) Fornasier et al. (2008), (18) Devogèle et al. (2018), (19) Arredondo et al. (2021), (20) DeMeo et al. (2009), (21) Reddy et al. (2014).

B–A frames. Finally, the reflectivity was obtained for both VIS and NIR data, dividing each asteroid spectrum by that of the SA star closest in time and airmass to the target. When nonSA stars were used for the telluric removal of a given target spectrum, we applied the following correction to derive the reflectivity relative to the Sun,  $R(\lambda)$ :

$$R(\lambda) = \frac{s_{ast}(\lambda)}{s_*(\lambda)} * F_c, \quad (2)$$

where  $s_{ast}$  is the asteroid spectrum and  $s_*$  is the nonG2V star spectrum. The  $F_c$  is the factor that allows the color of a given star to be corrected to that of the Sun, and is computed as follows:

$$F_c = \frac{s_*}{s_{G2V}}, \quad (3)$$

where  $s_{G2V}$  is the spectrum of a trusted G2V analog star observed during the night and relatively close in time to the star. To avoid spurious contributions in the  $F_c$  factor associated with telluric residuals, we first cut the main telluric bands residuals in  $F_c$ , replacing them by the linear fit of the data at the edges of a given band, and then we applied a median filter with a large window. This method turns out to be more efficient in reproducing the overall spectral behavior of the color-correction factor  $F_c$  than applying a polynomial fit. Finally, the spectra were normalized at 0.6  $\mu\text{m}$  for the data acquired in the VIS range, and at 1.0  $\mu\text{m}$  for those in the NIR range. We chose these normalization wavelengths because most of the visible spectra are reliable after 0.55  $\mu\text{m}$ , which is the wavelength commonly used in the literature for normalization, and they are not affected by telluric band residuals and outside inflection points of potential absorption bands. We also checked that the selected normalization wavelengths did not affect the taxonomic assignment. Finally, for a given asteroid, when both VIS and NIR data exist, we combined them together, following the method described later in Sect. 3.5.

### 3.4. Literature data

As previously mentioned, 56 out of 64 IMBPs have existing data in the literature: 28 have spectra in the VIS range, 24 in NIR, while 21 have spectra in both the VIS and NIR ranges. The majority of spectra come from the MITHNEOS IRTF survey (Binzel et al. 2019), which observed near-Earth and main belt asteroids in the VIS and NIR ranges, from the SMASS database (Sawyer 1991; Bus & Binzel 2002), and the  $S^3OS^2$  surveys (Lazzaro et al. 2004). Additional spectra were presented in several articles, and were retrieved using the Small Bodies Node Ferret database<sup>2</sup> or, when not available, were kindly provided by the authors of the papers. For asteroids with multiple spectra in the literature, we selected those with the highest S/N and the widest wavelength coverage. Details about the sources of the different IMBP spectra used for our study are reported in Table 3.

### 3.5. Spectral analysis

For each asteroid, when both VIS and NIR spectra exist (either from the literature or from the new observations presented here), we combined them in order to cover the full  $\sim 0.5\text{--}2.3$   $\mu\text{m}$  range. To do so, we first identified a common wavelength region to normalize each spectral part (usually around 0.88–0.90  $\mu\text{m}$ ). We then computed the average reflectance values of the VIS and NIR part of the spectrum around the common wavelength  $\pm 200$  Å

and normalized each part using these mean values. Additionally, visual inspection of the two spectral parts was performed to ensure that the normalization generated a consistent spectral behavior between the two parts. Finally, each full spectrum was normalized at 0.60  $\mu\text{m}$  for the spectral analysis. The spectra of the IMBPs that include new observations are reported in Figs. 2, 3, and 4, while those available in the literature are shown in Fig. A.1.

We taxonomically classified the spectra following the Bus-DeMeo taxonomy (DeMeo et al. 2009), using the M4AST tool<sup>3</sup> (Popescu et al. 2012). This tool compares asteroid spectra with the average ones of the different classes in the Bus-DeMeo classification using the least chi-squared method. Visual inspection was carefully performed to check the meaning of the proposed taxonomic type solutions, and eventually to identify absorption bands that are characteristic of some types. The results of the spectral classification are reported in Table 3.

We then computed the spectral slopes in several ranges, applying linear regressions (Fornasier et al. 2016):  $S_{\text{all}}$  for the whole spectral range;  $S_{\text{VIS}}$  for the VIS range, between 0.50 and 0.75  $\mu\text{m}$ ;  $S_{\text{NIR1}}$  in the 1.1–1.6  $\mu\text{m}$  range, and  $S_{\text{NIR2}}$  in the 1.7–2.2  $\mu\text{m}$  range. To characterize the absorption bands, we applied the method described in Gaffey et al. (1993). First, we calculated the linear continuum at the borders of a given band. We then divided the local spectrum by this continuum, and applied an  $N$ th order polynomial fitting (usually  $N$  is comprised between 3 and 8) to determine the absorption band parameters. For the band center, we looked at the wavelength value where the value of the first derivative of the polynomial function is equal to 0; the bandwidth is determined by the position of the two maxima around the studied band, and the band depth corresponds to the distance between the reflectance of the linear continuum and that of the center of the band. The spectral band parameters are reported in Tables 4 and B.2.

## 4. Results

### 4.1. Taxonomy of the IMBPs

After we performed the spectral classification, we identified that 43.75% of the total population of the IMBPs belong to the S-complex, 26.56% to the C-complex, 17.19% to the X-complex, and 12.50% are end members (see Fig. 5). The S-types dominate the S-complex population, whereas in the C-complex, the 69.00% are Ch/Cgh asteroids, which show absorption features produced by the aqueous alteration process. About half of the IMBPs belonging to the X-complex show an absorption in the 0.9  $\mu\text{m}$  region, which is typical of the Xk-type.

For the end member classes, the IMBP population includes two L-types (172 and 234), two D-types (72 and 732), two K-types (131, 186), one T-type (336), and one V-type (4). Figure 5B shows the taxonomic distribution of IMBPs against their diameter. S-complex IMBPs are found at various sizes, C-complex IMBPs have diameters in the 25–200 km range, and the X-complex IMBPs and L-, D-, and K-types are all smaller than 100 km.

Recently, Vernazza et al. (2021) investigated the shape of large asteroids and reported new density estimations. The following asteroids of our IMBP list were investigated by these authors: (4) Vesta, (6) Hebe, (7) Iris, (8) Flora, (9) Metis, (11) Parthenope, (12) Victoria, (18) Melpomene, (19) Fortuna, (21) Lutetia, (51) Nemausa, (63) Ausonia, and (230) Athamantis. The

<sup>2</sup> <https://sbnapps.psi.edu/ferret/>

<sup>3</sup> <http://m4ast.imcce.fr>

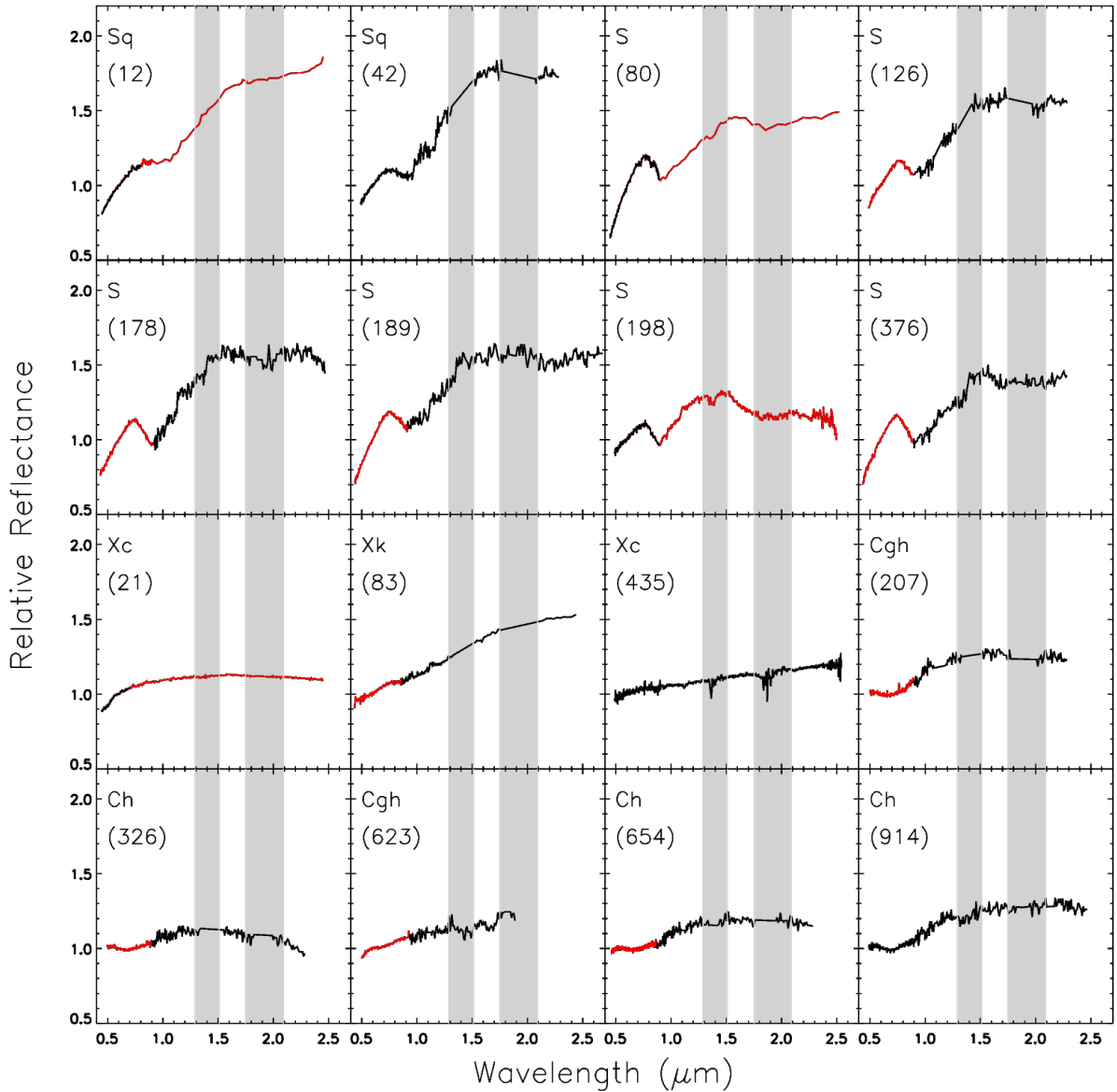


**Fig. 2.** Spectra of S-, C-, and X-complex planetesimals. New observations are shown in black, with the VIS or NIR data from the literature shown in red. Gray areas in the figures indicate the position of the main telluric absorption bands.

taxonomical classification is the same among their results and ours (see Table 1 of Vernazza et al. 2021), except for (12) Victoria, which they classified as A-type, while it is an Sq according to our observations (Fig. 2). More specifically, the VIS-NIR spectrum presented here does not show the 0.9  $\mu\text{m}$  band, which is typical of A-types.

We also investigated the IMBP VIS spectral slope versus the visible geometric albedo  $p_V$  of the asteroids (Fig. 6). We observed an expected trend with three distinct regions: one including the C-complex bodies, showing low albedo and low spectral slope values, one populated by S-complex asteroids with medium to high albedo and high spectral slope values, and, finally, one for the X-complex bodies, which includes both low- and medium-albedo asteroids with moderate spectral slope values (with the notable exception of (44) Nysa which is the brightest IMBP). Surprisingly, Xc-type asteroids show albedo variability, including both dark and relatively bright surfaces. As expected, D-type IMBPs have low  $p_V$ -values and high spectral slopes. Interestingly, Vernazza et al. (2021) found a dichotomy in

the density distribution versus albedo for C- and S-type bodies in their large asteroid shape survey, with low-albedo C-type bodies having densities lower than 2  $\text{g/cm}^3$  and high-albedo bodies having densities beyond 2.5  $\text{g/cm}^3$ .

We finally investigated the mass distribution of the IMBPs (Fig. 7). For most of them, we used the mass value from Carry (2012) and from the MP3C when the mass is not reported in the former publication. However, 18 planetesimals do not have mass determination in the literature, and thus we estimated the mass ( $M$ ) of these bodies from Eq. (4):

$$M = \frac{\pi}{6} \rho D^3, \quad (4)$$

where  $\rho$  is the density of the object and  $D$  its diameter. For the density, we took the estimated values from Carry (2012) for each taxonomic class. Following the approach of DeMeo & Carry (2014), we calculated the amount of mass per spectral type or per complex in three different size ranges (Fig. 7). We then compared our results for the planetesimal population with those of

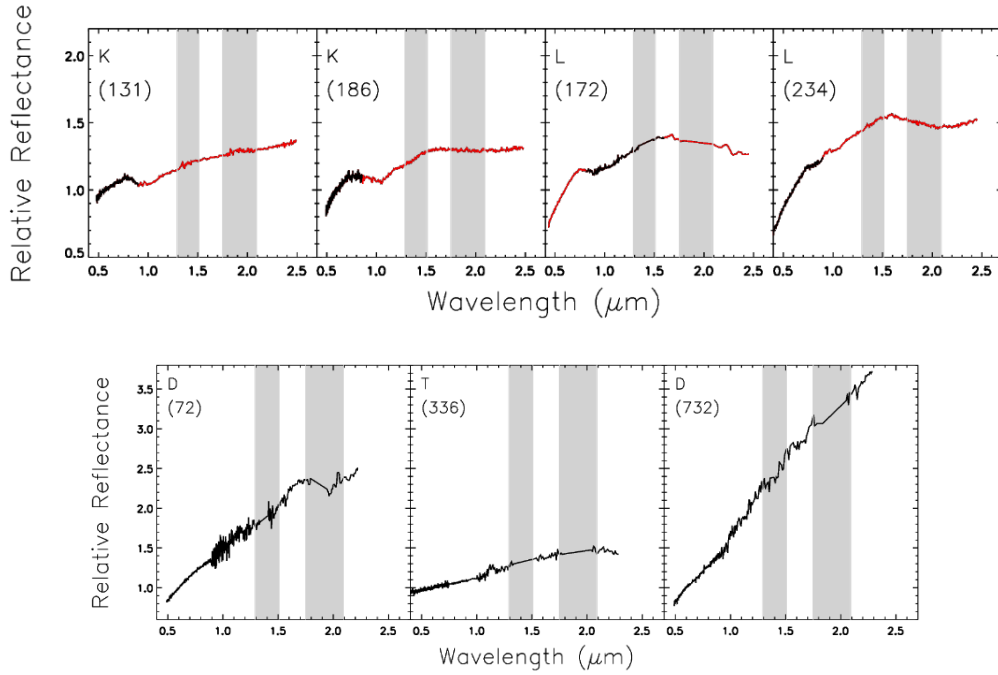


**Fig. 3.** Spectra of K- and L-type (*top*) and D/T-type (*bottom*) planetesimals. The new observations are presented in black, completed with the VIS or NIR data from the literature in red.

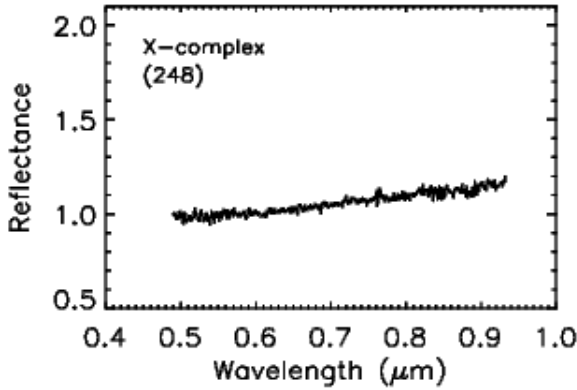


**Fig. 4.** Visible spectrum of the X-type (248) Lameia (no NIR data are available for this object).

DeMeo & Carry (2014) – who focus on asteroids – regardless of their origin (planetesimals and collisional fragments). In this comparison, it should be noted that DeMeo & Carry (2014) used the Tholen taxonomy (Tholen 1984), while our analysis is based on the Bus-DeMeo taxonomy. Most of the taxonomic classes are the same among the two taxonomies, with the notable exception of X-complex bodies, which are classified as E-, M-, and P-type in Tholen taxonomy and as X, Xc, Xk, Xe, and Xn in the Bus-DeMeo taxonomy, and aqueously altered asteroids, which have deviated types (Ch/Cgh) in Bus-DeMeo taxonomy while they are classified as C-types in the Tholen one. The planetesimal versus asteroids mass distribution (Fig. 7) shows that:

– For the planetesimals with a diameter greater than 100 km, the presence of (4) Vesta largely dominates (76.2%) over the other objects. This result is consistent with that of DeMeo & Carry (2014). For the other classes, we found more or less the same distributions as those reported by DeMeo & Carry (2014), namely S-complexes represent 20.1% of the total mass of the IMBPs, followed by the C-complexes, which represent 3.7%.

**Table 4.** Band parameters of S-type IMBPs.

Object	BII / BI Area	BI center (μm)	ol/(ol + pyr) (%)
(6) Hebe	0.750 ± 0.001	0.917 ± 0.002	54.49 ± 0.02
(7) Iris	0.457 ± 0.003	0.957 ± 0.011	61.74 ± 0.07
(8) Flora	0.664 ± 0.003	1.021 ± 0.007	56.72 ± 0.08
(9) Metis <sup>(†)</sup>	0.557 ± 0.002	1.082 ± 0.008	59.33 ± 0.05
(11) Parthenope	0.305 ± 0.001	0.948 ± 0.006	65.42 ± 0.02
(17) Thetis	1.655 ± 0.005	0.912 ± 0.002	32.75 ± 0.12
(18) Melpomene	1.080 ± 0.013	0.904 ± 0.005	46.66 ± 0.32
(20) Massalia	0.921 ± 0.001	0.914 ± 0.001	50.51 ± 0.02
(27) Euterpe	0.547 ± 0.004	0.960 ± 0.008	59.56 ± 0.10
(40) Harmonia	0.577 ± 0.002	0.916 ± 0.002	58.84 ± 0.05
(42) Isis <sup>(†)</sup>	0.082 ± 0.004	0.951 ± 0.001	70.82 ± 0.10
(63) Ausonia	0.713 ± 0.001	0.943 ± 0.006	55.55 ± 0.03
(67) Asia	0.853 ± 0.008	0.914 ± 0.002	52.16 ± 0.19
(79) Eurynome	0.543 ± 0.005	0.932 ± 0.002	59.66 ± 0.12
(80) Sappho	0.447 ± 0.011	0.940 ± 0.012	61.98 ± 0.03
(118) Peitho	1.009 ± 0.002	0.910 ± 0.001	48.38 ± 0.05
(126) Velleda <sup>(†)</sup>	0.202 ± 0.046	0.974 ± 0.010	67.91 ± 1.12
(138) Tolosa	0.598 ± 0.002	1.045 ± 0.007	58.33 ± 0.05
(178) Belisana <sup>(†)</sup>	0.145 ± 0.001	0.938 ± 0.009	69.29 ± 0.02
(182) Elsa	0.929 ± 0.007	0.918 ± 0.002	50.32 ± 0.17
(192) Nausikaa	0.638 ± 0.001	0.994 ± 0.007	57.36 ± 0.03
(198) Ampella	1.208 ± 0.027	0.897 ± 0.003	43.57 ± 0.65
(298) Baptistina	0.748 ± 0.009	1.026 ± 0.011	54.70 ± 0.22
(376) Geometria <sup>(†)</sup>	0.267 ± 0.001	0.947 ± 0.014	66.35 ± 0.02
(556) Phyllis	0.623 ± 0.011	0.918 ± 0.003	57.72 ± 0.27

**Notes.** Band parameters of S-complex planetesimals calculated following the Gaffey et al. (1993) method. The olivine over olivine/pyroxene ratio was computed using Eq. (5) from Dunn et al. (2010). Objects with <sup>(†)</sup> were analyzed by our own code, the others using the M4AST tool.

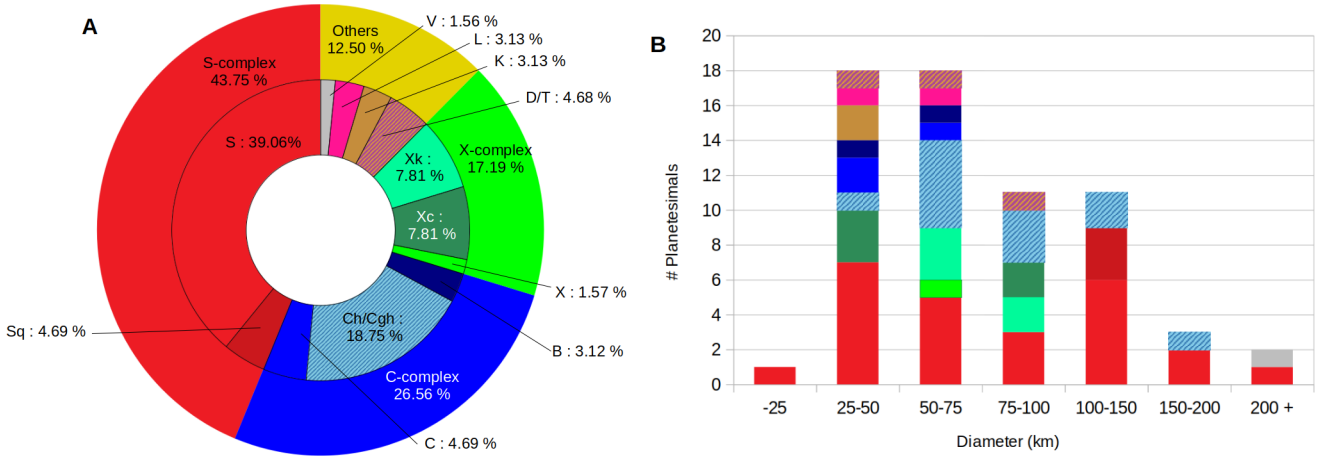


**Fig. 5.** Distribution of taxonomical classes of the IMBPs. (A) Proportion of planetesimals among the four main complexes of the Bus-DeMeo taxonomy (S, C, X, and end members, noted as Others in the pie charts) and subclasses; (B) histogram of the distribution in size of all IMBPs, with the same color code as that used for the taxonomic classes.

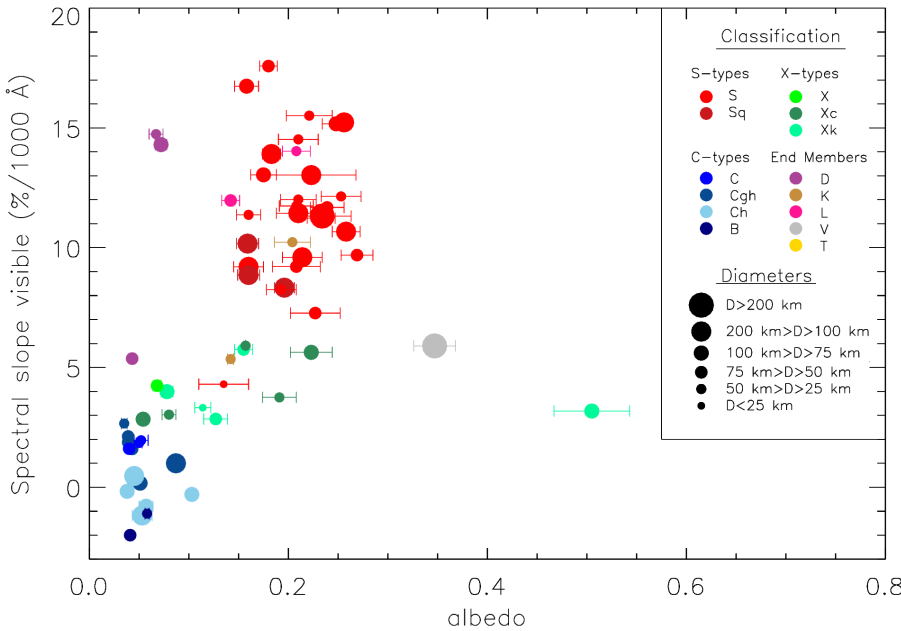


**Fig. 6.** Distribution of the visible spectral slope versus the albedo for the IMBPs. Uncertainties on spectral slope values are smaller than the symbols size.

– For the planetesimals with a diameter in the 50–100 km range, we observed a clearly different distribution from that found by DeMeo & Carry (2014): C-complex IMBPs, and in particular those in the Ch and Cgh classes, clearly dominate the population. These latter represent one-third of the total mass of the planetesimals in this size range. We also found that only 25.0% of the mass of the IMBPs belongs to the S-complex. On the other hand, DeMeo & Carry (2014) found that the S-complex represents almost 50.0% of 50–100 km asteroids in the inner main belt. No important differences in the distribution of X-complex asteroids and IMBPs were seen. However, we found a non-negligible fraction of D/T types, accounting for 12.7% of the mass of IMBPs, whereas in DeMeo & Carry (2014) such types do not appear for diameters between 50 and 100 km.

– For objects smaller than 50 km in diameter, S-complex IMBPs dominate, but in smaller proportions compared to the general asteroids reported by DeMeo & Carry (2014): only 42.9% of the total mass in this size range of the planetesimals compared to the 50.0% of the mass of all asteroids

(DeMeo & Carry 2014). Planetesimals also include an important fraction (~20.0% in mass) of L-types. On the other hand, C-complex planetesimals are less present compared to the rest of the inner main belt asteroids. Finally, the distributions of X-complex planetesimals and asteroids in general are also quite similar in this size range.

#### 4.2. Mineralogical characterization

Next, we studied the surface mineralogy of the IMBPs. This characterization is based on the identification of absorption features at particular wavelengths that are known to be associated with a given mineralogy.

##### 4.2.1. S-complex IMBPs

To compute the spectral band parameters of S-complex IMBPs, we mostly used the M4AST (Popescu et al. 2012) online tool, but we also developed an IDL code to compute them. This code was

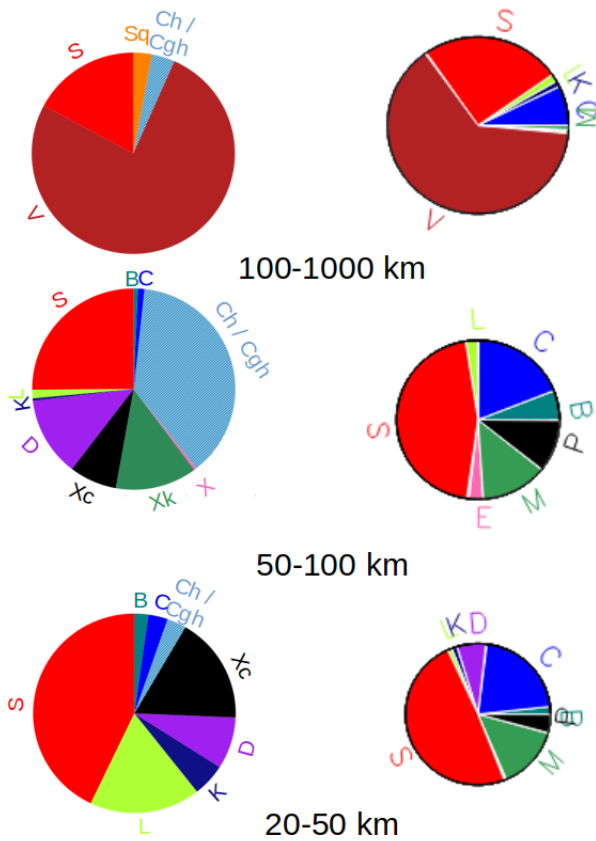


**Fig. 7.** Distribution in mass of the IMBPs with diameter between 20 and 1000 km (*left*) and distribution in mass of all the inner main belt asteroids from the paper of DeMeo & Carry (2014) (*right*). For the planetesimals, we use the Bus&Demeo taxonomy, while DeMeo & Carry (2014) used the Tholen one. Therefore, X, Xk, and Xc classes on the left side should be compared with the E, M, and P ones on the right, while Ch/Cgh-types fall within the C-class in the Tholen taxonomy.

applied to double check the results provided by M4AST. Both the online tool and our code follow the methodology described in Cloutis et al. (1986) for band parameter computation. We, thus, determined the center, depth, and area for the two absorption features, characteristics of silicates (Table 4). These features are centered at  $\sim 1 \mu\text{m}$  and  $\sim 2 \mu\text{m}$ , and named BI and BII bands, respectively, following the Gaffey et al. (1993) classification scheme. Both bands are present for asteroids whose composition is dominated by pyroxene, while, in general, only the BI band is present for olivine-rich bodies. The BII band may vary in depth between objects, depending on the ratio between olivine and pyroxene. Namely, if  $\text{BII/BI} = 0$ , the mineralogy is dominated by olivine, whereas, if  $2.8 > \text{BII/BI} > 1.6$ , the asteroid is dominated by pyroxene. Gaffey et al. (1993) identified seven subgroups of the S-complex, ranging from olivine-rich bodies S(I) to the pyroxene-rich ones S(VII), with a progressive increase in pyroxene abundance from subgroups I to VII. We show the regions corresponding to these seven S-subclasses in Fig. 8, where the BI center versus the BII over BI band area is represented. For some spectra, the BII is not well defined due to the fact that the spectrum had to be cut before  $2.50 \mu\text{m}$ , because of the instrumental detection limit and/or low S/N. Therefore, in order to characterize the BII area, we fitted the existing data with a polynomial of the order of between 5 and 7, and we extended the spectrum to  $2.50 \mu\text{m}$  using the fitted data. We measured the BII/BI area

ratio (hereafter referred to as the band area ratio (BAR); values are reported in Table 4) for the S-complex IMBPs analyzed here (Fig. 8), except for those with only the visible spectrum. To estimate the uncertainties, we fitted the bands using a polynomial of order  $n_{\text{fit}} \pm 2$ , where  $n_{\text{fit}}$  is the order that better reproduces a given absorption band, and we considered the standard deviation of the spectral parameters derived using the aforementioned polynomial.

Apart from the asteroid family parents, the majority of the IMBPs studied here are intact primordial objects and therefore the effects of space weathering should be important, implying that band depth decreases up to 50.00% according to Clark et al. (2002) and Gaffey (2010). Under the assumption that the space weathering effects are similar in both the BI and BII bands, and considering that we plot the band ratio, space weathering effects should nevertheless not affect the  $x$ -axis of the plot, but may shift the BI center position towards shorter wavelengths according to Sasaki & Kurahashi (2001) and Britt et al. (2014).

Using the bands areas, we estimated the proportion of olivine in the olivine–pyroxene mixtures characterizing the S-complex planetesimals (Table 4) using the formula from Dunn et al. (2010):

$$\frac{\text{ol}}{\text{ol} + \text{pyr}} = -0.242 \times \text{BAR} + 0.728. \quad (5)$$

Figure 8 summarizes the results for the S-complex IMBPs. Most of them are located inside the red area corresponding to the subtype S(IV) of Gaffey et al. (1993), and are characterized by a mineralogy similar to that of the ordinary chondrites. The second-most populated region is the one of the S(III) subgroup. According to Gaffey et al. (1993), this subgroup represents the most varied one, where the mineralogy includes calcic pyroxene components with important BAR variation, meaning various amounts of olivine. The planetesimal (138) Tolosa falls in the S(II) subgroup, which is characterized by a mineralogy dominated by olivine with a non-negligible amount of calcic pyroxene contents. Only (17) Thetis has a deep BII band and falls in the S(VII) group, meaning that its mineralogy could correspond to a pyroxene-dominated or a basaltic assemblage (Gaffey et al. 1993). Table 4 reports the results of the olivine/pyroxene ratio, which indeed confirm the distribution of the IMBPs represented in Fig. 4: (17) Thetis, which falls in the pyroxene-dominated area, shows 32.75% olivine, while (42) Isis shows 70.82% olivine in the mixture. On average, S-complex IMBPs contain 56.81% olivine in the olivine/pyroxene ratio.

#### 4.2.2. C-complex IMBPs

Among the carbon-rich IMBPs, we find that 12 out of 17 objects show features associated with aqueous alteration. This process is the chemical alteration of minerals produced by liquid water in the planetesimal during its formation (Fornasier et al. 2014). This process results in an absorption band around  $2.7\text{--}3.0 \mu\text{m}$  due to water molecules and to the OH ion present in the mineral crystal lattice (Lebofsky 1980; Rivkin et al. 2002; Howell et al. 2011; Takir & Emery 2012). This feature is often accompanied by a fainter absorption band in the visible region, the most common one being a broad absorption feature ( $0.30 \mu\text{m}$  wide) centered around  $0.70 \mu\text{m}$ , produced by  $\text{Fe}^{2+} \rightarrow \text{Fe}^{3+}$  charge transfer in the phyllosilicate minerals (Vilas 1994; Barucci et al. 1998; Fornasier et al. 1999). In the literature, a strong correlation (Vilas et al. 1993; Vilas 1994; Fornasier et al. 2014; Rivkin et al. 2015) has been found between the  $\sim 3 \mu\text{m}$  and  $0.70 \mu\text{m}$

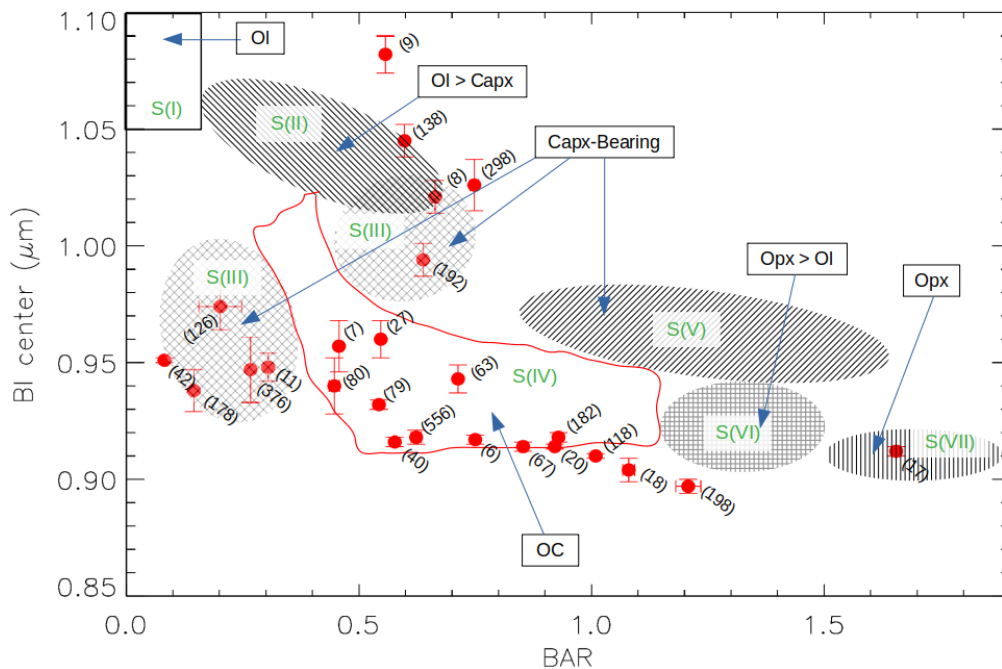


**Fig. 8.** Plot of the Band I center vs. BAR for the S-complex IMBPs. The different ellipses and polygons represent the main mineralogy of the various S-complex subgroups defined by Gaffey et al. (1993). OI: monomineralic olivine, Capx: calcipyroxene, OC: mafic silicate components of ordinary chondrite, Opx: orthopyroxene.

bands: almost all the asteroids showing the 0.70  $\mu\text{m}$  band also present the 3  $\mu\text{m}$  band, while sometimes the 3  $\mu\text{m}$  absorption is not accompanied by the 0.70  $\mu\text{m}$  one, because this last is much fainter and may be cooked out by thermal processes, or possibly masked by the noise of the data. For the 12 aqueous-altered IMBPs investigated here, the band depth varies between 1.25% and 5.00%, which is consistent with the result from the survey of Fornasier et al. (2014). All are taxonomically classified as Cgh- or Ch-types, which is expected because these classes are defined by the presence of the 0.70  $\mu\text{m}$  band. Their diameter is greater than  $\sim 50$  km, in agreement with the work of Fornasier et al. (2014), who found that the aqueous alteration process dominates in carbonaceous asteroids starting from 2.3 au and for objects with a diameter of greater than 50 km. We did not find a correlation between the semimajor axis and the 0.7  $\mu\text{m}$ -band depth for the hydrated C-complex IMPBs. The percentage of hydrated asteroids is higher at shorter distances from the Sun: 100% of the C-complex asteroids are hydrated in the 2.20–2.40 au, while the percentage decreases to 50% between 2.40 and 2.50 au, although it should be noted that we have a relatively small sample (17 C-complex planetesimals). This result indicates that the 0.7  $\mu\text{m}$ -band was not baked out at closer heliocentric distances in the IMB carbonaceous asteroids. As discussed in the following section, the presence of hydrated carbonaceous asteroid supports migration theories and their implantation in the IMB from larger heliocentric distances.

#### 4.2.3. X-complex and end-member IMBPs

The mineralogy of X-complex IMBPs is diverse, as they do not show the same features among the different types. X-complex objects have been associated with metal-rich, enstatite-rich and carbon-rich mineralogies, and were classified as M-, E-, and P-types in the former Tholen taxonomy.

In our survey, Xk-type planetesimals show a band in the 0.8–1.0  $\mu\text{m}$  region due to the presence of low-calcium, low-iron orthopyroxene, with depth varying between 2.00% and 4.00% which is consistent with values reported in the literature (Fornasier et al. 2011). For the other X-complex planetesimals, and specifically for the X- and Xc-types, the study of the surface mineralogy is limited because of the absence of absorption bands in the VIS and NIR ranges.

Regarding the end members, there are two D-types and one T-type, which are characterized by a very red and featureless spectrum with an average slope in the VIS–NIR range of 11.00%/1000  $\text{\AA}$ . This red spectral behavior is commonly associated with an organic-rich composition of the surface (Gradie & Veveřka 1980; Emery & Brown 2004).

The L-type (172) Baucis and (234) Barbara show a wide band around 2.0  $\mu\text{m}$  due to FeO-bearing content in the spinel mineral, one of the main species of the calcium–aluminum inclusion (CAI; Sunshine et al. 2008; Devogèle et al. 2018). Therefore, L-type asteroids could contain the very first minerals formed in the Solar System (Devogèle et al. 2018). K-types have spectra intermediate between S- and C-type. The 1.0  $\mu\text{m}$  band is wider than that in the S-complex, and the NIR range is characterized by a flat spectrum (Bus & Binzel 2002; Clark et al. 2009; DeMeo et al. 2009). This class appears to have a carbon-rich surface, as spectral parameters of the 1.0  $\mu\text{m}$  band are similar to those of carbonaceous meteorites. In our study, the 1.0  $\mu\text{m}$ -band depth of the two K-type IMBPs is around 6.00%, which is consistent with the values measured by Clark et al. (2009).

#### 4.3. Comparison with meteorites and minerals

For the planetesimals with the full 0.5–2.3  $\mu\text{m}$  coverage, we also performed a spectral matching with meteorite laboratory spectra. To identify the best matches, we used the M4AST tool (Popescu et al. 2012), which utilizes the RELAB database

of meteorites and minerals (Pieters 1983). The tool performs curve matching via the least chi-square method between the asteroid and the meteorite sample to select the best-matching analogs. Additionally, we visually inspected the spectra of the best-matched meteorites and minerals, which should reproduce the observed absorption features in the spectrum of the asteroid, if any. We also considered the albedo or reflectance of the asteroid or meteorite to select the best match. For dark asteroids (i.e.  $p_V < 10\%$ ), we considered meteorites and minerals with a reflectance value equal to the asteroid albedo, namely  $\pm 3\%$ , while for those with  $p_V > 10\%$ , we considered matches with reflectance equal to the asteroid albedo  $\pm 5\%$ , following the same approach adopted by Fornasier et al. (2011). This was done in order to take into account the difference in geometry and surface roughness between asteroids and laboratory measurements. Results are reported in Fig. A.2 and in Table B.2.

We find that the majority of S-complex planetesimals were best matched, as expected, by ordinary chondrite (OC), in particular the L6 type ( $\sim 34\%$  of OC L6 among all the S-complex IMBPs). This result confirms the major overlap between the S-complex IMBPs and the OC zone in Fig. 8. However, our study shows that the asteroids (11), (17), (126), and (298), which are located outside the OC region in Fig. 8, are also currently best matched by ordinary chondrites. The fact that some S-type planetesimals are associated with a laser-irradiated OC indicates that space weathering processes should be important on their surfaces.

Of the 12 Ch and Cgh-type planetesimals, 7 are best matched by the CM2 carbonaceous chondrites. These meteorites are associated with aqueous altered asteroids in the literature (Fornasier et al. 1999, 2014). Their metamorphic grade 2 on the Van Schmus and Wood scale (Van Schmus & Wood 1967) reveals an important aqueous alteration. Additionally, (329) Svea is, according to the literature, also related to a CM chondrite (Fornasier et al. 2014).

The X-complex IMBPs cannot be all matched with the existing meteorites in the RELAB database. The ones that can get a link are associated to either enstatite chondrites, mesosiderites or CM carbonaceous meteorites, as it has been suggested already in the literature (Vernazza et al. 2009; Avdellidou et al. submitted) confirming that the X-complex is highly variable in composition.

Finally, the L-type planetesimals (172) Baucis and (186) Celuta are best fitted by CV3 carbonaceous chondrites. The link between L-type asteroids and CV3/CO3 meteorites has already been reported in the literature (Mothé-Diniz et al. 2005; Devogèle et al. 2018).

For featureless and red sloped IMBPs, the spectral matches are usually inconclusive. For instance, the D-type (72) Feronia is matched by sulphide troilite from the Canyon Diablo iron meteorite, while the D/T-type planetesimal (336) Lacadiera has a good match with a CM2 carbonaceous chondrite. For the other D-type, (732) Tjilaki, we did not find any satisfactory match.

For 13 of the IMBPs, the meteorite matches were indeed very good and the spectral behavior very similar. This is the case for (27) Euterpe, (79) Eurynome, and (376) Geometria, which are all similar to the laser-irradiated OC Château Renard L6 sample; and (67) Asia and (182) Elsa, which both match the Dhajala OC H3.4 sample. Other very good matches are: (4) Vesta with HED meteorites, as expected (Keil 2002); (7) Iris with an OC L3 meteorite; (44) Nysa with an enstatite oldhamite sample; (135) Hertha with an iron meteorite; (313) Chaldaea with the CM2 Murchinson meteorite; (435) Ella with the Abee enstatite meteorite, and (623) Chimaera with the Tagish Lake carbonaceous meteorite.

For these bodies, we can assume a mineralogy similar to that of the meteorite best matched.

## 5. Discussion

### 5.1. Missing taxonomies

First of all, we noted that A-, R-, O-, and Q-types are missing amongst the IMBPs. The detection of an A-type amongst IMBPs could potentially be interesting, as this taxonomical class characterizes either olivine-rich asteroids that are supposed to originate from the exposure – following collisional breakup for example – of the mantle of a differentiated parent body (DeMeo et al. 2019, and references therein) or asteroids formed through nebular processes (Sunshine et al. 2007; Sanchez et al. 2014). In the very first spectroscopic studies, few A-type asteroids were identified, which gave rise to the so-called missing mantle problem in the main belt. Even if some authors hypothesized that olivine-rich A-type asteroids should be more abundant in the main belt than observed (Bell 1988), recent extended spectroscopic surveys confirm the small number of A-type objects identified. DeMeo et al. (2019) concluded that the missing mantle problem is a fact and that asteroid differentiation is not as important as previously thought. In fact, DeMeo et al. (2019) found that A-type asteroids represent only a mere  $p = 0.16\%$  of the main belt asteroid population. Therefore, the probability  $P$  of detecting one or more A-types amongst IMBPs is given by Eq. (6)

$$P = \sum_{k=1}^n \binom{n}{k} p^k (1-p)^{n-k}, \quad (6)$$

where  $n = 64$  is the number of IMBPs and  $\binom{n}{k}$  is the binomial coefficient. We found that  $P = 9.70\%$ , hence quite unlikely to happen. On the other hand, if we consider that there are 3 A-types among the 608 main belt asteroids with a diameter of larger than 50 km, which is 0.49% of the population,  $P$  becomes equal to 27.00%. It is therefore still quite unlikely to see one A-type among the IMBPs.

The absence of Q-types is somehow expected as planetesimals are old and therefore highly space weathered, while Q-type asteroids are supposed to have undergone rejuvenating processes including a *peel off* scenario (Binzel et al. 2010; Nesvorný et al. 2010) or the Yarkovsky-YORP effects that could remove the weathered regolith from their surface (Polishook et al. 2014; Graves et al. 2018). Finally, concerning the R- and O-types, their absence among the IMBPs can be explained by the fact that these spectroscopic types are also very rare within the asteroid population, and therefore the chance of detecting one in a sample of 64 asteroids is quite small.

### 5.2. S-complex

According to our results, it appears that the mineralogy of the majority of S-complex IMBPs is related to the ordinary chondrites (OCs). This relationship is also strengthened by the fact that we found that OCs of subtype L offer the best spectroscopic match with S-complex IMBPs. The link between S-complex asteroids and OC meteorites is nowadays well established, notably thanks to in situ measurement of the Hayabusa mission on the S-complex asteroid (25143) Itokawa and the detailed laboratory measurements on its samples brought back to Earth (Nakamura et al. 2011; Yurimoto et al. 2011). However, it is worth remembering that before the year 2000, this link was not

yet well established (Gaffey 1984; Bell 1988; Gaffey et al. 1989, 1993; Lipschutz et al. 1989), because S-type asteroids were found to be systematically spectrally redder than the ordinary chondrite spectra. This conundrum was solved when space-weathering processes were shown to explain the differences between the spectra of asteroids and those of the OC meteorites (see Brunetto & Strazzulla 2005, and references therein).

Vernazza et al. (2014) predicted formation areas according to the subtype of OC: for high-pyroxene-content meteorites (H chondrite), the source region is predicted around the 3:1 mean motion resonance with Jupiter, that is,  $\sim 2.5$  au, while for those with a high olivine content (L and LL chondrites) the source is preferentially closer to the Sun, around the  $\nu_6$  secular resonance at low orbital inclination (2 au) or the Mars crossing region ( $< 2$  au). For this reason, we investigated whether or not there is a dependence between the olivine/pyroxene abundance ratio and the proper semi-major axis of S-complex IMBPs. We find a Pearson correlation coefficient of  $-0.02$  between the semi-major axis of the S-complex IMBPs and the olivine/pyroxene abundance ratio, with a probability of 0.91, meaning that there is no correlation between the two quantities. We also find no correlation between the size of IMBPs and their olivine/pyroxene abundance ratio: the correlation coefficient is  $-0.006$  with a significance of 0.97. Our data therefore do not support a current heliocentric dependence of the olivine/pyroxene abundance ratio of S-complex IMBPs. It is therefore likely that the semi-major axis of S-complex IMBPs was scrambled by dynamical effects. For instance, these bodies could have been implanted in the main belt during the early phases of Solar System evolution (Walsh et al. 2011; Raymond & Izidoro 2017a,b) from a source region partially overlapping with the current inner main belt and also stretching to lower heliocentric distances.

### 5.3. C-complex and Ch/Cgh types

Here, we show that objects of the C-, S-, and X-complex are present within the population of IMBPs. From Table B.2, we also note that S-complex IMBPs are in general associated with non-carbonaceous chondrite meteorites (NCs), mostly OCs, whereas C-complex IMBPs can be linked to carbonaceous chondrite meteorites (CCs). In addition, X-complex IMBPs contain bodies that can be associated with both NCs (those with high albedo) and CCs (those with low albedo). Hence, the parent bodies of NCs and CCs are found in a 0.4 au-wide region of the Solar System, with orbital semi-major axis between 2.1 and 2.5 au. On the other hand, laboratory measurements have shown that NCs and CCs form two distinct groups in anomalies of nucleosynthetic isotopes (Warren 2011; Budde et al. 2016). Moreover, it has also been claimed that NCs and CCs sample two reservoirs of materials that coexisted, but have been kept spatially separated for several million years after the beginning of our Solar System (Kruijjer et al. 2017; Lichtenberg et al. 2021), the latter being set at 4.567 Gyr ago by the dating of the CAIs present in some chondrites (Amelin 2020). In order to keep the two reservoirs separated, Kruijjer et al. (2017) proposed that the formation of Jupiter acted as a barrier against material exchange between the reservoirs of NCs and CCs; alternatively, Brassier & Mojzsis (2020) suggested that the separation between the two reservoirs was due to a pressure maximum in the disk near the location where Jupiter was about to be born. The only possible scenario capable of reconciling our astronomical observations with meteorite isotopic anomaly measurements is that mixing of the NC and the CC parent bodies happened at the later stage of the early Solar System evolution, that is, after the IMBPs were fully

accreted. Our results corroborate the paradigm that planetesimal mixing probably occurred before the collisional evolution of asteroids and the formation of their collisional families.

Another piece of potential evidence that the C-complex IMBPs were transported to the inner main belt region from elsewhere is that the majority of them are aqueously altered (Ch and Cgh-types). This implies that liquid water was present in the early formation phases of these bodies. The presence of aqueously altered asteroids in the inner main belt observed here was already reported in literature (Fornasier et al. 2014), where objects much smaller than the IMBPs are collisional fragments originating from these parent bodies. Recent studies of primitive, carbon-rich, inner-main-belt collisional families reported aqueous alteration in the Erigone and Sulamitis families (Morate et al. 2018, 2019), thus corroborating our results. Additionally, both the near-Earth asteroids Benu and Ryugu, targets of the sample-return missions OSIRIS-Rex and Hayabusa 2, of NASA and JAXA, respectively, showed evidence of aqueous alteration (Hamilton et al. 2019; Kitazato et al. 2019). As it has also been shown that Benu and Ryugu are collisional fragments of parent bodies located in the inner main belt (Bottke et al. 2015; Campins et al. 2013), this further substantiates the presence of aqueously altered IMBPs located between 2.1 and 2.5 au from the Sun.

Cgh and Ch types are usually linked to CM2 carbonaceous chondrites, which are aqueously altered (Fornasier et al. 2014; Rivkin et al. 2015; Landsman et al. 2015; Potin et al. 2020). Our spectroscopic matching between meteorites and IMBPs confirms this link with CM2 CCs. Alexander et al. (2018) estimated that the CM2 meteorite parent bodies (and more generally carbonaceous chondrites) were formed at 3–7 au from the Sun. This implies that aqueously altered IMBPs formed at greater heliocentric distances than their present position and were then later implanted in the inner main belt (2.1–2.5 au), where we observe them today. Vernazza et al. (2021) propose, on the basis of their density estimates and spectrophotometric observations, that many main belt C-type asteroids could come from the Kuiper Belt region and that their surface represents the aqueously altered evolution of P- and D-type-like material.

Different dynamical models can explain the transport of C-complex IMBPs from their formation location – at 3–7 au for example – to the inner main belt, such as the so-called Grand Tack (Walsh et al. 2011), and the low-mass asteroid belt model (Raymond & Izidoro 2017a,b).

### 5.4. D-types

We find two D-types amongst our sample of IMBPs, namely (72) Feronia, with  $D = 78.8 \pm 2.0$  km, and (732) Tjilaki, with  $D = 33.7 \pm 0.3$  km, and one T-type, (336) Lacadiera, with  $D = 69.8 \pm 0.7$  km. Levison et al. (2009) showed that D-type asteroids could be the results of implantation of scattered objects from the primordial transneptunian region, while Kwon et al. (2022) propose that T-type asteroids might originate from beyond the main belt but closer than the Kuiper region, that is at a distance of around 10 au. Additionally, Vernazza et al. (2021) found, through their survey, that D-/P-type asteroids share a common origin with Centaurs, short-period comets, and small TNOs. These authors also suggest that some C-complex and D-/P-type asteroids could represent layers of the same body, with C-type composition coming from the core and P/D-type composition from the outer shell. Their implantation in the current main belt happened during the giant planet orbital instability. The initial work of Levison et al. (2009) is not able to explain the presence of objects with spectra

similar to those of transneptunian objects (D-types) in the inner main belt, because the capture efficiency of their model was virtually null for this region. On the other hand, the presence of D-types in the inner main belt was already noted by DeMeo et al. (2014). These authors proposed a scenario that they also claimed to be quite unlikely: that these objects were transported by the nongravitational Yarkovsky effect from the central main belt to the inner main belt. However, the secular semimajor axis drift due to the Yarkovsky effect is very small for these large D-types, and so they would not be able to cross the 3:1 mean motion resonance with Jupiter in order to move from the central to the inner part of the main belt.

Nevertheless, Vokrouhlický et al. (2016) revised the implantation model of Levison et al. (2009) with an updated version of the giant planet instability, showing that transneptunian objects could indeed have also been captured in the inner part of the main belt. Vokrouhlický et al. (2016) estimated a number of  $5_{-2}^{+5}$  D-type asteroids with a diameter of greater than 30 km in the inner main belt, which is consistent with our observational findings.

## 6. Conclusions

We identified 64 asteroids of the inner main belt ( $2.1 < a < 2.5$  au) that (i) stand outside V-shapes of collisional families, (ii) are the parent bodies of the collisional asteroid families themselves, or (iii) are large interlopers of these families, and therefore cannot be considered members of them. As such, these bodies cannot be considered collisional fragments that formed in the main belt from the fragmentation of a parent body. Following the previous logic of Delbo et al. (2017), we consider these 64 asteroids to be IMBPs that formed from the accretion of solids in the protoplanetary disk of our Sun.

We used literature data and performed novel spectroscopic observations to characterize the composition and physical properties of these IMBPs. We show that 43.8% of the IMBPs in our sample belong to the S-complex, followed by C-complex planetesimals (~26.6%), X-complex (~17.2%), and end members (~12.5%). In terms of mass, in the  $D > 100$  km size range, (4) Vesta dominates, followed by S-complex IMBPs and by a small fraction of hydrated (Ch/Cgh types) C-complex IMBPs (Fig. 7). This is consistent with the previous findings of DeMeo et al. (2014). However, these authors did not distinguish the contribution of hydrated objects. On the other hand, in the  $50 < D < 100$  km size range, we find that the Ch and Cgh classes clearly dominate the IMPB population, with only 25.0% in mass in S-complex. Our results are therefore different from those of DeMeo et al. (2014) who found that the S-complex represents almost 50.0% of the asteroids in the inner main belt. The difference is because DeMeo and co-authors did not distinguish between collisional fragments and planetesimals. Hence, the compositional gradient found by DeMeo et al. (2014) is not primordial, but is affected by the asteroid collisional evolution, a problem that we avoid in the present study.

While a dependence between the olivine to pyroxene ratio and the heliocentric distance of the formation of bodies is expected from cosmological arguments (Vernazza et al. 2014), this dependence is not observed in our analysis. It is therefore likely that the semi-major axis of S-complex IMBPs was scrambled by dynamical effects. One of these could be that these bodies were implanted in the main belt during the early phases of Solar System evolution (Walsh et al. 2011; Raymond & Izidoro 2017a,b). Our finding of the presence of Ch/Cgh, D, and T type IMBPs can also be explained by the giant-planet-migration

models (Walsh et al. 2011; Raymond & Izidoro 2017a,b), as these planetesimals should be formed in the outer part of the Solar System (beyond 3 au) (Raymond & Izidoro 2017b; Alexander et al. 2018) and be transported to their current orbital semi-major axes later.

We observed no A-type or Q-type IMBPs. While this is likely due to a bias inherent to the small number of IMBPs and the small abundance of these classes throughout the main belt, it is also possible that the lack of A-type and Q-type IMBPs could be due to the nature of these spectroscopic classes: A-types are interpreted as olivine-rich asteroids produced by the fragmentation of a differentiated parent body. As IMBPs are not asteroid fragments created in the main belt, it is therefore logical that we do not find A-types among them. Q-types represent bodies with fresh surfaces, and resemble the OCs in their spectroscopy. It is therefore natural not to find Q-types amongst IMBPs, which are as old as our Solar System and therefore should have highly space-weathered surfaces.

*Acknowledgements.* We acknowledge support from the ANR ORIGINS (ANR-18-CE31-13-0014). This work made use of observations collected at the Copernico telescope (Asiago, Italy) of the Istituto Nazionale di Astrofisica (INAF) – Osservatorio Astronomico di Padova, at the Italian Telescopio Nazionale Galileo (TNG) operated on the island of La Palma, Spain, by the Centro Galileo Galilei of INAF, and at the Lowell Discovery Telescope at Lowell Observatory. Lowell is a private, non-profit institution dedicated to astrophysical research and public appreciation of astronomy and operates the LDT in partnership with Boston University, the University of Maryland, the University of Toledo, Northern Arizona University and Yale University. This work is based on data provided by the Minor Planet Physical Properties Catalogue (MP3C) of the Observatoire de la Côte d’Azur. This research has made use of the Small Bodies Data Ferret (<http://sbn.psi.edu/ferret/>), supported by the NASA Planetary System. This project has received funding from the European Union’s Horizon 2020 research and innovation programme under grants agreement No 101004719 and No 730890. C.A. and M.D. were Visiting Astronomers at the Infrared Telescope Facility, which is operated by the University of Hawaii under contract 80HQTR19D0030 with the National Aeronautics and Space Administration. Part of the data utilized in this publication were obtained and made available by the MITHNEOS MIT-Hawaii Near-Earth Object Spectroscopic Survey. We thank the anonymous referee for all the comments and suggestions which helped us to improve this article.

## References

- Alexander, C. M. O., McKeegan, K. D., & Altwegg, K. 2018, *Space Sci. Rev.*, **214**, 36
- Amelin, Y. 2020, in *Oxford Research Encyclopedia of Planetary Science* (Oxford University Press), 133
- Arredondo, A., Campins, H., Pinilla-Alonso, N., et al. 2021, *Icarus*, **358**, 114210
- Asphaug, E., Agnor, C. B., & Williams, Q. 2006, *Nature*, **439**, 155
- Aydellidou, C., Delbo, M., Morbidelli, A., et al., *Sci. Adv.*, submitted
- Baffa, C., Comoretto, G., Gennari, S., et al. 2001, *A&A*, **378**, 722
- Banase, K., Crane, P., Grosbol, P., et al. 1983, *The Messenger*, **31**, 26
- Barucci, M. A., Doressoundiram, A., Fulchignoni, M., et al. 1998, *Icarus*, **132**, 388
- Barucci, M. A., Fornasier, S., Dotto, E., et al. 2008, *A&A*, **477**, 665
- Barucci, M. A., Perna, D., Popescu, M., et al. 2018, *MNRAS*, **476**, 4481
- Bell, J. F. 1988, *Meteoritics*, **23**, 256
- Bell, J. F., Owensby, P. D., Hawke, B. R., et al. 2005, *NASA Planetary Data System*, EAR
- Binzel, R. P., Morbidelli, A., Merouane, S., et al. 2010, *Nature*, **463**, 331
- Binzel, R. P., DeMeo, F. E., Turtelboom, E. V., et al. 2019, *Icarus*, **324**, 41
- Bolin, B. T., Delbo, M., Morbidelli, A., & Walsh, K. J. 2017, *Icarus*, **282**, 290
- Botke, W. F., Durda, D. D., Nesvorný, D., et al. 2005, *Icarus*, **179**, 63
- Botke, W. F., Vokrouhlický, D., Walsh, K. J., et al. 2015, *Icarus*, **247**, 191
- Brasser, R., & Mojzsis, S. J. 2020, *Nat. Astron.*, **4**, 492
- Britt, D., Kohout, T., Schelling, P., & Consolmagno, G. J. 2014, in *AAS/Division for Planetary Sciences Meeting Abstracts*, **46**, 506.01
- Brunetto, R., & Strazzulla, G. 2005, *Icarus*, **179**, 265
- Budde, G., Burkhardt, C., Brennecka, G. A., et al. 2016, *Earth Planet. Sci. Lett.*, **454**, 293
- Bus, S. J., & Binzel, R. P. 2002, *Icarus*, **158**, 146
- Campins, H., de León, J., Morbidelli, A., et al. 2013, *AJ*, **146**, 26

- Carry, B. 2012, *Planet. Space Sci.*, **73**, 98
- Clark, B. E., Hapke, B., Pieters, C., & Britt, D. 2002, in *Asteroids III*, eds. W. F. Bottke, A. Cellino, P. Paolicchi, & R. P. Binzel (Tucson: Univ. Arizona Press), 585
- Clark, B. E., Bus, S. J., Rivkin, A. S., Shepard, M. K., & Shah, S. 2004, *AJ*, **128**, 3070
- Clark, B. E., Ockert-Bell, M. E., Cloutis, E. A., et al. 2009, *Icarus*, **202**, 119
- Cloutis, E. A., Gaffey, M. J., Jackowski, T. L., & Reed, K. L. 1986, *J. Geophys. Res.*, **91**, 11,641
- Cushing, M. C., Vacca, W. D., & Rayner, J. T. 2004, *PASP*, **116**, 362
- Cuzzi, J. N., Hogan, R. C., & Shariff, K. 2008, *ApJ*, **687**, 1432
- Deianno, R., Walsh, K. J., & Delbo, M. 2021, *Icarus*, **357**, 114218
- Delbo, M., Walsh, K., Bolin, B., Avdellidou, C., & Morbidelli, A. 2017, *Science*, **357**, 1026
- Delbo, M., Avdellidou, C., & Morbidelli, A. 2019, *A&A*, **624**, A69
- DeMeo, F. E., & Carry, B. 2014, *Nature*, **505**, 629
- DeMeo, F. E., Binzel, R. P., Slivan, S. M., & Bus, S. J. 2009, *Icarus*, **202**, 160
- DeMeo, F. E., Binzel, R. P., Carry, B., Polishook, D., & Moskovitz, N. A. 2014, *Icarus*, **229**, 392
- DeMeo, F. E., Polishook, D., Carry, B., et al. 2019, *Icarus*, **322**, 13
- Dermott, S. F., Christou, A. A., Li, D., Kehoe, T. J. J., & Robinson, J. M. 2018, *Nat. Astron.*, **2**, 549
- Devogèle, M., Tanga, P., Cellino, A., et al. 2018, *Icarus*, **304**, 31
- Dunn, T. L., McCoy, T. J., Sunshine, J. M., & McSween, H. Y. 2010, *Icarus*, **208**, 789
- Dykhuis, M. J., & Greenberg, R. 2015, *Icarus*, **252**, 199
- Emery, J. P., & Brown, R. H. 2004, *Icarus*, **170**, 131
- Fieber-Beyer, S. K., Gaffey, M. J., Hardersen, P. S., & Reddy, V. 2012, *Icarus*, **221**, 593
- Fornasier, S., Lazzarin, M., Barbieri, C., & Barucci, M. A. 1999, *A&As*, **135**, 65
- Fornasier, S., Migliorini, A., Dotto, E., & Barucci, M. A. 2008, *Icarus*, **196**, 119
- Fornasier, S., Clark, B. E., Dotto, E., et al. 2010, *Icarus*, **210**, 655
- Fornasier, S., Clark, B. E., & Dotto, E. 2011, *Icarus*, **214**, 131
- Fornasier, S., Lantz, C., Barucci, M. A., & Lazzarin, M. 2014, *Icarus*, **233**, 163
- Fornasier, S., Lantz, C., Perna, D., et al. 2016, *Icarus*, **269**, 1
- Gaffey, M. J. 1984, *Icarus*, **60**, 83
- Gaffey, M. J. 2010, *Icarus*, **209**, 564
- Gaffey, M. J., Bell, J. F., & Cruikshank, D. P. 1989, in *Asteroids II*, eds. R. P. Binzel, T. Gehrels, & M. S. Matthews (Tucson: Univ. of Arizona Press), 98
- Gaffey, M. J., Bell, J. F., Brown, R. H., et al. 1993, *Icarus*, **106**, 573
- Gerbig, K., Murray-Clay, R. A., Klahr, H., & Baehr, H. 2020, *ApJ*, **895**, 91
- Gradie, J., & Tedesco, E. 1982, *Science*, **216**, 1405
- Gradie, J., & Veverka, J. 1980, *Nature*, **283**, 840
- Graves, K. J., Minton, D. A., Hirabayashi, M., DeMeo, F. E., & Carry, B. 2018, *Icarus*, **304**, 162
- Gustafsson, A., Moskovitz, N., Cushing, M. C., et al. 2021, *PASP*, **133**, 035001
- Hamilton, V. E., Simon, A. A., Christensen, P. R., et al. 2019, *Nat. Astron.*, **3**, 332
- Hardersen, P. S., Cloutis, E. A., Reddy, V., Mothé-Diniz, T., & Emery, J. P. 2011, *MaPS*, **46**, 1910
- Howell, E. S., Rivkin, A. S., Vilas, F., et al. 2011, in *EPSC-DPS Joint Meeting*, 637
- Johansen, A. 2015, in *Encyclopedia of Astrobiology*, eds. M. Gargaud, W. M. Irvine, R. Amils, I. Cleaves, Henderson James (Jim), D. L. Pinti, J. C. Quintanilla, D. Rouan, T. Spohn, S. Tirard, & M. Viso (Springer), 1035
- Keil, K. 2002, in *Asteroids III*, eds. W. F. Bottke Jr., A. Cellino, P. Paolicchi, & R. P. Binzel (Tucson: University of Arizona Press), 573
- Kelley, M. S., & Gaffey, M. J. 2000, *Icarus*, **144**, 27
- Kitazato, K., Milliken, R. E., Iwata, T., et al. 2019, *Science*, **364**, 272
- Klahr, H., & Schreiber, A. 2020, *ApJ*, **901**, 54
- Kruijer, T. S., Burkhardt, C., Budde, G., & Kleine, T. 2017, *Proc. Natl. Acad. Sci. U.S.A.*, **114**, 6712
- Kwon, Y. G., Hasegawa, S., Fornasier, S., Ishiguro, M., & Agarwal, J. 2022, *A&A*, in press <https://doi.org/10.1051/0004-6361/202243816>
- Landsman, Z. A., Campins, H., Pinilla-Alonso, N., Hanuš, J., & Lorenzi, V. 2015, *Icarus*, **252**, 186
- Lazzaro, D., Angeli, C. A., Carvano, J. M., et al. 2004, *Icarus*, **172**, 179
- Lebofsky, L. A. 1980, *AJ*, **85**, 573
- Levison, H. F., Bottke, W. F., Gounelle, M., et al. 2009, *Nature*, **460**, 364
- Lichtenberg, T., Drążkowska, J., Schönbächler, M., Golabek, G. J., & Hands, T. O. 2021, *Science*, **371**, 365
- Lipschutz, M. E., Gaffey, M. J., & Pellas, P. 1989, in *Asteroids II*, eds. R. P. Binzel, T. Gehrels, & M. S. Matthews (Tucson: Univ. Arizona Press), 740
- Morate, D., de León, J., De Prá, M., et al. 2018, *A&A*, **610**, A25
- Morate, D., de León, J., De Prá, M., et al. 2019, *A&A*, **630**, A141
- Mothé-Diniz, T., Roig, F., & Carvano, J. M. 2005, *Icarus*, **174**, 54
- Nakamura, T., Noguchi, T., Tanaka, M., et al. 2011, *Science*, **333**, 1113
- Nesvorný, D., Bottke, W. F., Vokrouhlický, D., Chapman, C. R., & Rafkin, S. 2010, *Icarus*, **209**, 510
- Nesvorný, D., Brož, M., & Carruba, V. 2015, in *Asteroids IV*, eds. P. Michel et al. (Tucson: Univ. of Arizona Press), 297
- Pieters, C. M. 1983, *J. Geophys. Res.*, **88**, 9534
- Polishook, D., Moskovitz, N., Binzel, R. P., et al. 2014, *Icarus*, **233**, 9
- Popescu, M., Birlan, M., & Nedelcu, D. A. 2012, *A&A*, **544**, A130
- Potín, S., Beck, P., Usui, F., et al. 2020, *Icarus*, **348**, 113826
- Raymond, S. N., & Izidoro, A. 2017a, *Icarus*, **297**, 134
- Raymond, S. N., & Izidoro, A. 2017b, *Sci. Adv.*, **3**, e1701138
- Rayner, J. T., Toomey, D. W., Onaka, P. M., et al. 2003, *PASP*, **115**, 362
- Reddy, V., & Sanchez, J. A. 2016, *NASA Planetary Data System*, EAR
- Reddy, V., Sanchez, J. A., Bottke, W. F., et al. 2014, *Icarus*, **237**, 116
- Reynolds, C. M., Reddy, V., & Gaffey, M. J. 2009, in *40th Annual Lunar and Planetary Science Conference*, Lunar and Planetary Science Conference, 1285
- Rivkin, A. S., Howell, E. S., Vilas, F., & Lebofsky, L. A. 2002, *Hydrated Minerals on Asteroids: The Astronomical Record*, 235
- Rivkin, A. S., Thomas, C. A., Howell, E. S., & Emery, J. P. 2015, *AJ*, **150**, 198
- Sanchez, J. A., Reddy, V., Kelley, M. S., et al. 2014, *Icarus*, **228**, 288
- Sasaki, S., & Kurahashi, E. 2001, in *AAS/Division for Planetary Sciences Meeting Abstracts*, 33, 59.07
- Sawyer, S. R. 1991, *Bull. Am. Astron. Soc.*, **23**, 1235
- Scott, E. R. D., Keil, K., Goldstein, J. I., et al. 2015, in *Asteroids IV*, eds. P. Michel et al. (Tucson: Univ. of Arizona Press), 573
- Spoto, F., Milani, A., & Knežević, Z. 2015, *Icarus*, **257**, 275
- Sunshine, J. M., Bus, S. J., Corrigan, C. M., McCoy, T. J., & Burbine, T. H. 2007, *MaPS*, **42**, 155
- Sunshine, J. M., Connolly, H. C., McCoy, T. J., Bus, S. J., & La Croix, L. M. 2008, *Science*, **320**, 514
- Takir, D., & Emery, J. P. 2012, *Icarus*, **219**, 641
- Tanga, P., Delbo, M., & Gerakis, J. 2013, in *AAS/Division for Planetary Sciences Meeting Abstracts*, 45, 208.29
- Tholen, D. J. 1984, PhD thesis, University of Arizona, USA
- Tomasella, L., Benetti, S., Chiomento, V., et al. 2016, Afosc @ 1.82m Copernico Telescope - User manual
- Van Schmus, W. R., & Wood, J. A. 1967, *Geochim. Cosmochim. Acta*, **31**, 747
- Vernazza, P., Binzel, R. P., Rossi, A., Fulchignoni, M., & Birlan, M. 2009, *Nature*, **458**, 993
- Vernazza, P., Zanda, B., Binzel, R. P., et al. 2014, *ApJ*, **791**, 120
- Vernazza, P., Ferrais, M., Jorda, L., et al. 2021, *A&A*, **654**, A56
- Vilas, F. 1994, *Icarus*, **111**, 456
- Vilas, F., Hiroi, T., & Zolensky, M. E. 1993, in *Lunar and Planetary Science Conference, Lunar and Planetary Science Conference*, 1465
- Vokrouhlický, D., Brož, M., Bottke, W. F., Nesvorný, D., & Morbidelli, A. 2006, *Icarus*, **182**, 118
- Vokrouhlický, D., Bottke, W. F., & Nesvorný, D. 2016, *AJ*, **152**, 39
- Walsh, K. J., Morbidelli, A., Raymond, S. N., O'Brien, D. P., & Mandell, A. M. 2011, *Nature*, **475**, 206
- Walsh, K. J., Delbó, M., Bottke, W. F., Vokrouhlický, D., & Lauretta, D. S. 2013, *Icarus*, **225**, 283
- Warren, P. H. 2011, *Geochim. Cosmochim. Acta*, **75**, 6912
- Xu, S., Binzel, R. P., Burbine, T. H., & Bus, S. J. 1995, *Icarus*, **115**, 1
- Yurimoto, H., Abe, K.-i., Abe, M., et al. 2011, *Science*, **333**, 1116

Appendix A: Additional figures

Fig. A.1: Spectra from literature

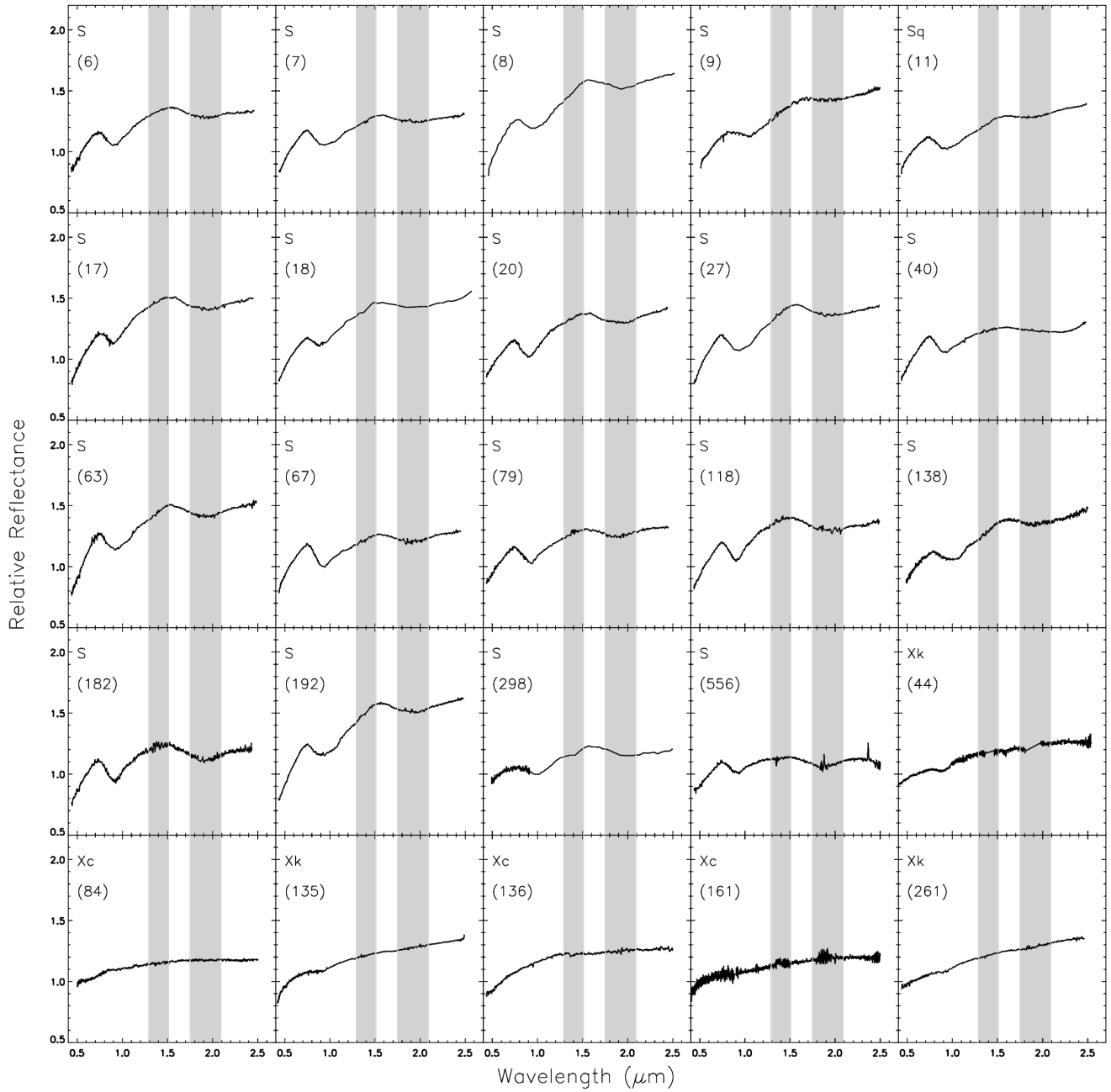


Fig. A.1: continued

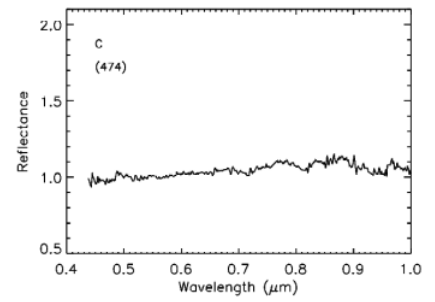
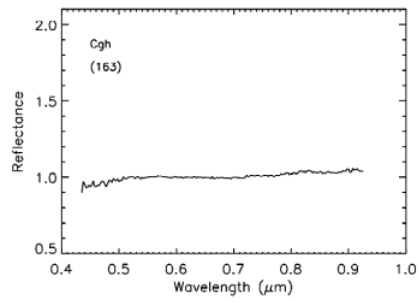
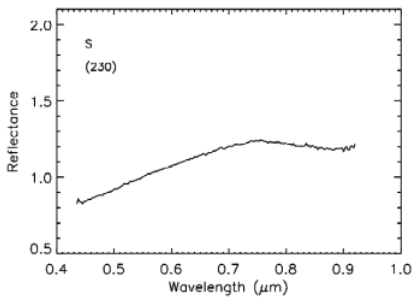
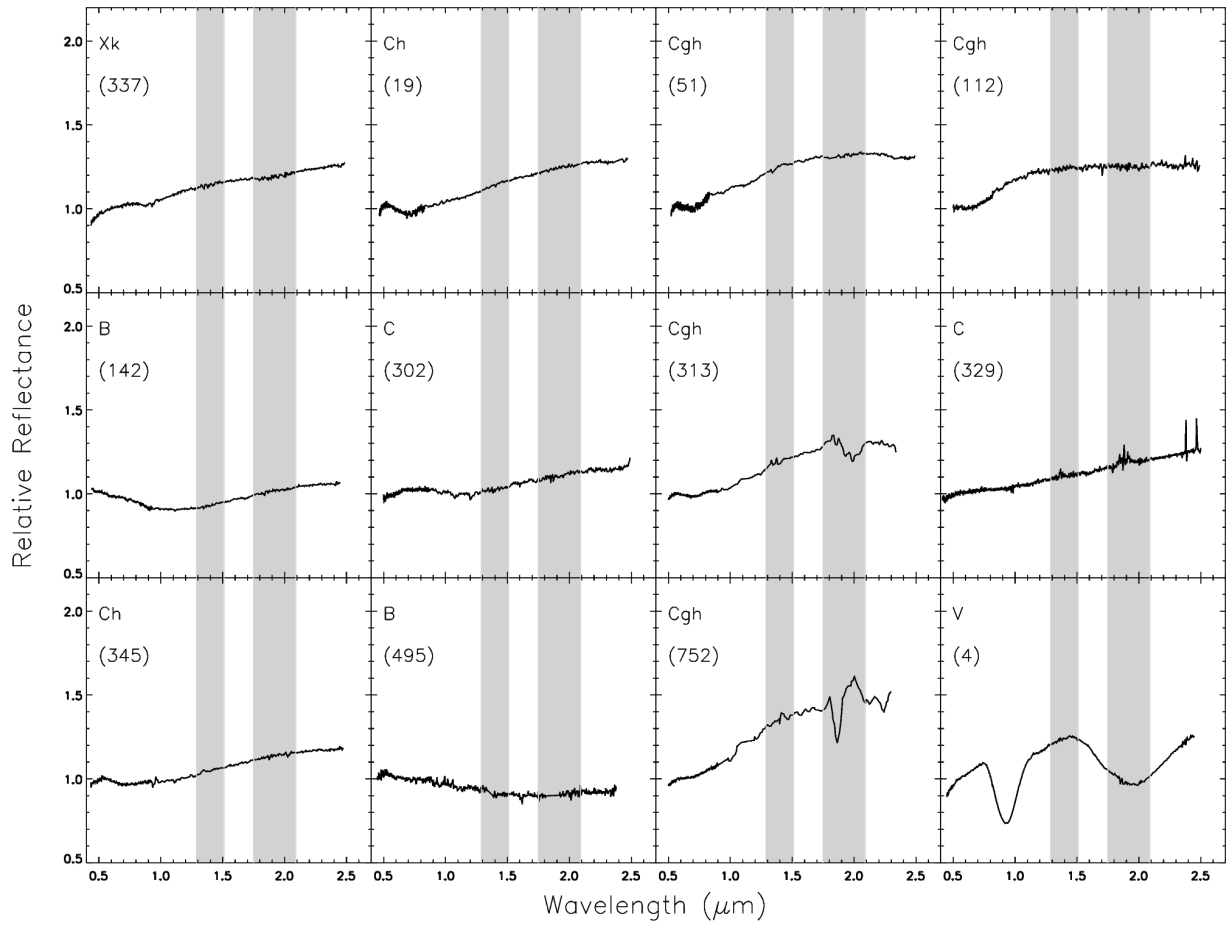


Fig. A.2: Comparison with RELAB database

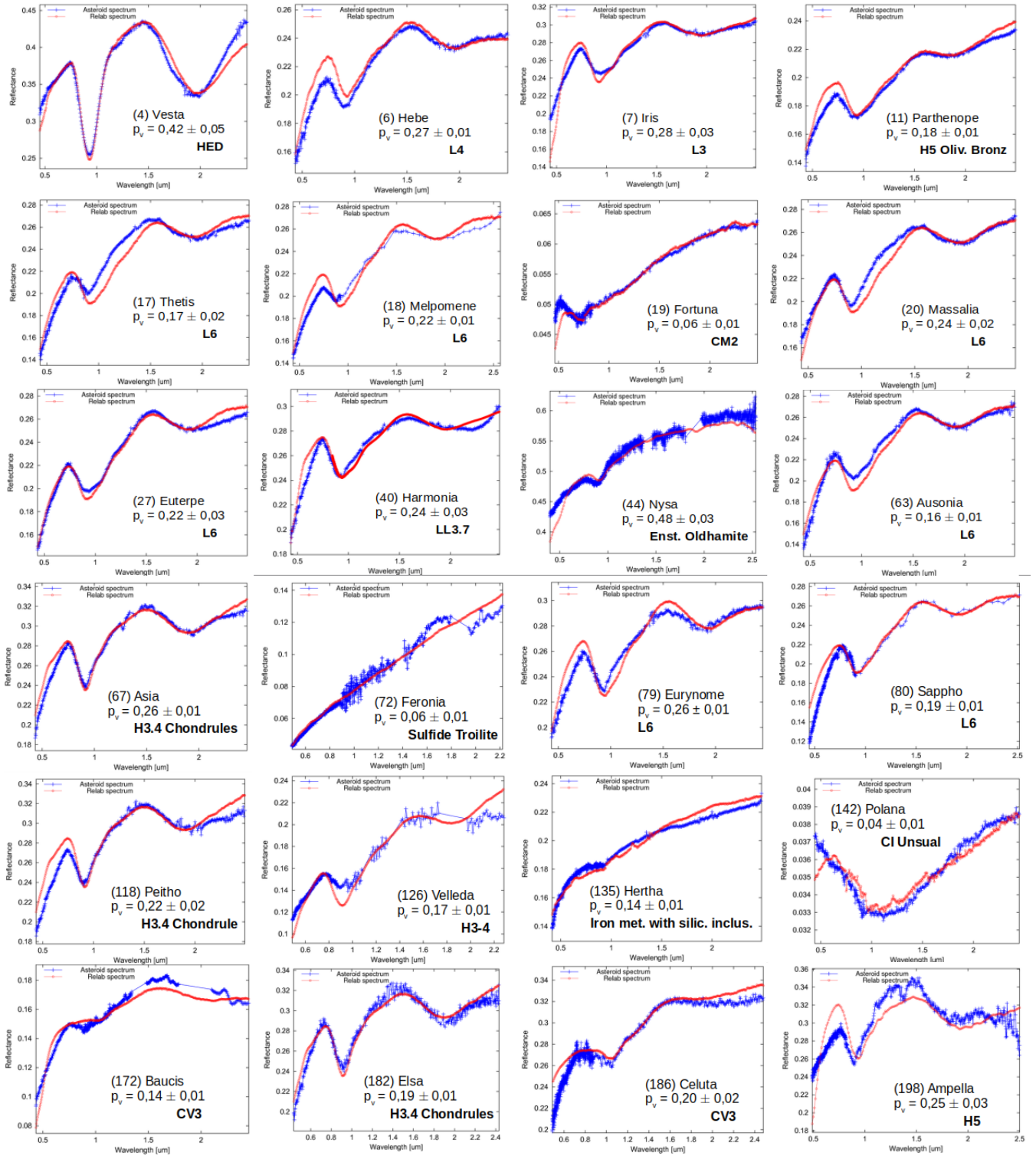
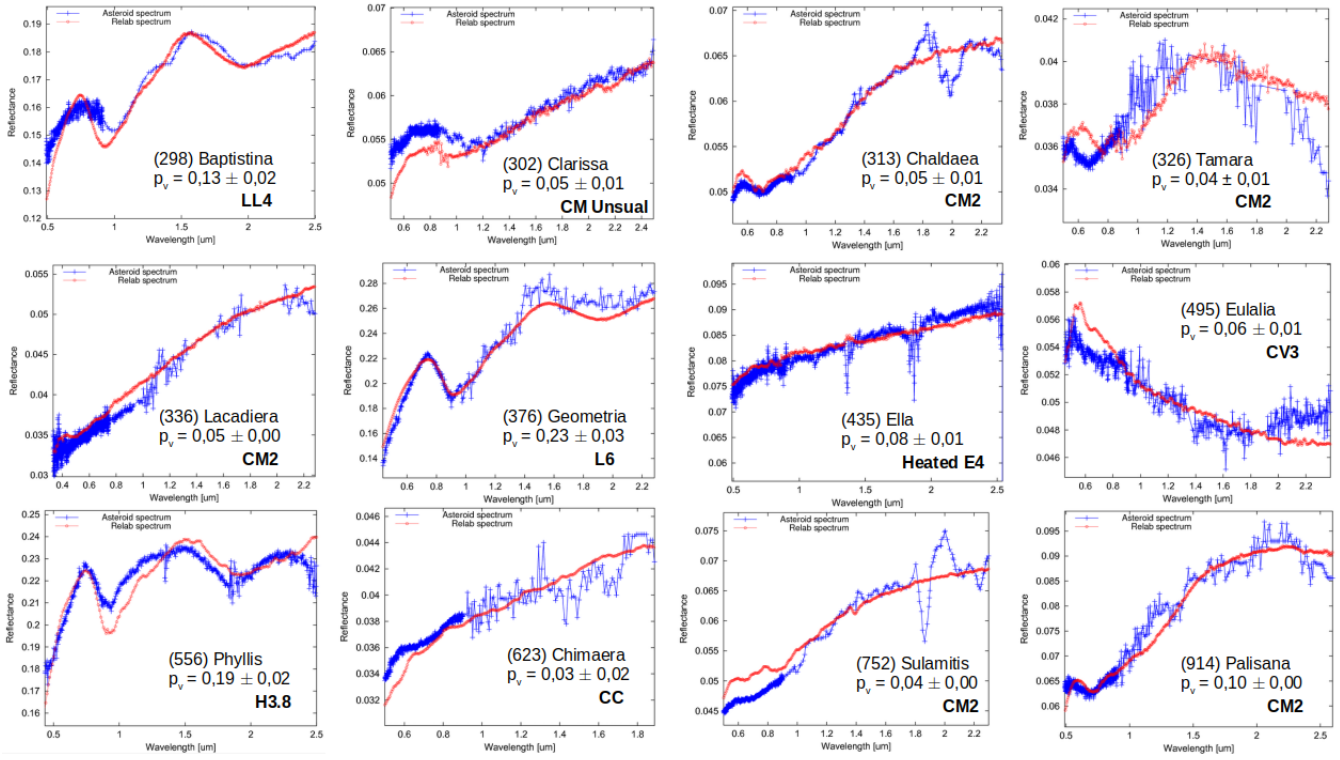


Fig. A.2: continued



**Notes :** A RELAB comparison was carried out for full spectra only. The planetesimal spectra are in blue and the best meteorite analog match is in red. More details are present in Table B.2.

**Appendix B: Additional tables**

Table B.1: MITHNEOS data references used in this paper

Asteroid Name	run #	UT date(s)
(4) Vesta	sp86	19 November 2009
(6) Hebe	sp68	10 March 2008
(7) Iris	sp28	19,20 February 2004
(9) Metis	sp75	31 October 2008
(11) Parthenope	sp47	12,13 November 2005
(17) Thetis	sp96	6 January 2011
(19) Fortuna	sp49	27,28 January 2006
(20) Massalia	sp96	6 January 2011
(21) Lutetia	sp76	3 December 2008
(27) Euterpe	sp31	22 September 2004
(40) Harmonia	sp32	16,17 October 2004
(63) Ausonia	sp25	30 September - 01 October 2003
(67) Asia	sp111	28 August 2012
(79) Eurynome	sp75	31 October 2008
(118) Peitho	sp102	25 September 2011
(142) Polana	sp86	19 November 2009
(192) Nausikaa	sp50	30 April - 1 May 2006
(234) Barbara	sp57	22 December 2006
(261) Pymno	sp64	2,3 October 2007
(302) Clarissa	sp233	26,28 July 2017
(345) Tercidina	sp45	8 October 2005

Table B.2: Band parameters and meteorite matching.

#	Name	Band Center ( $\mu\text{m}$ )	Band Width ( $\mu\text{m}$ )	Band Depth (%)	RELAB Comparison	RELAB file
4	Vesta	0.93	0.75-1.32	33.22	HED	camp74
		1.94	1.44-2.43	22.59		
6	Hebe	0.92	0.73-1.49	11.37	OC L4 Irradiated	c1oc15d15
		1.92	1.53-2.43	4.69		
7	Iris	0.96	0.73-1.51	12.69	OC L3	camb84
		1.98	1.58-2.48	4.48		
8	Flora	1.02	0.78-1.55	10.75	No Corresp.	-
		1.94	1.56-2.43	5.05		
9	Metis	1.08	0.81-1.50	9.04	OC H,L,LL or CO/CV (1)	-
		2.07	1.67-2.44	3.15		
11	Parthenope	0.95	0.73-1.56	11.59	OC H5 Olivine-Bronzite	cimh53
		1.93	1.54-2.26	2.98		
12	Victoria	1.05	0.82-1.55	9.63	No Corresp.	-
17	Thetis	0.91	0.74-1.48	10.32	OC L6 Irradiated	c1oc11d35
		1.96	1.59-2.42	6.30		
18	Melpomene	0.90	0.75-1.50	9.78	OC L6 Irradiated	c1oc11d35
		2.00	1.50-2.31	3.14		
19	Fortuna	0.70	0.52-0.83	5.04	CC CM2	c3mb62
20	Massalia	0.91	0.74-1.48	14.12	OC L6 Irradiated	c1oc11d35
		1.97	1.57-2.33	5.93		
21	Lutetia	-	-	-	CC CV3/CO3 (2) EC EL (8)	-
27	Euterpe	0.96	0.73-1.55	15.01	OC L6 Irradiated	c1oc11d35
		1.95	1.58-2.48	5.42		
40	Harmonia	0.92	0.74-1.57	10.99	OC LL3.7	bkr1mt156a
		2.21	1.61-2.46	4.73		
42	Isis	0.95	0.74-1.60	13.80	No Corresp	-
		2.06	1.70-2.23	2.11		
44	Nysa	0.90	0.76-1.00	3.42	Enstatite Oldhamite	c1tb61
51	Nemausa	0.71	0.57-0.83	4.88	CC CII or CM2 (3)	-
63	Ausonia	0.94	0.73-1.50	14.23	OC L6 Irradiated	c1oc11d35
		1.94	1.53-2.46	7.17		
67	Asia	0.91	0.75-1.53	15.41	OC H3.4 Chondrules	c1dp12
		1.91	1.55-2.29	4.82		
72	Feronia	-	-	-	Sulfide Troilite	laea01a
79	Eurynome	0.93	0.74-1.52	12.45	OC L6 Irradiated	c1oc11d35
		1.88	1.55-2.16	4.64		
80	Sappho	0.94	0.77-1.52	15.97	OC L6 Irradiated	c1oc11d35
		1.85	1.67-2.20	4.53		
83	Beatrix	1.06	0.78-1.13	2.78	No Corresp.	-
84	Klio	-	-	-	No Corresp.	-
112	Iphigenia	0.66	0.56-0.81	2.37	No Corresp.	-
118	Peitho	0.91	0.74-1.47	14.14	OC H3.4 Chondrules	c1dp12
		1.98	1.51-2.47	6.53		
126	Velleda	0.97	0.75-1.46	15.04	OC H3-4	cclm26
		1.97	1.71-2.14	4.88		
131	Vala	0.97	0.78-1.18	5.96	No Corresp.	-
135	Hertha	0.91	0.78-1.04	1.79	Iron Met. with silicate inc.	c1mb46
136	Austria	-	-	-	No Corresp.	-
138	Tolosa	1.03	0.79-1.62	10.98	No Corresp.	-
		1.90	1.62-2.32	3.82		
142	Polana	-	-	-	CC CI Unusual	ncmb19
161	Athor	-	-	-	ECs EL (4)	-
163	Erigone	0.70	0.57-0.83	2.42	No Corresp.	-
172	Baucis	0.90	0.75-1.14	4.11	CC CV3	bkr1mp130
178	Belisana	0.94	0.75-1.54	20.26	No Corresp.	-
		1.92	1.58-2.22	4.53		

Table B.2: continued

#	Name	Band Center ( $\mu\text{m}$ )	Band Width ( $\mu\text{m}$ )	Band Depth (%)	RELAB Comparison	RELAB file
182	Elsa	0.92	0.72-1.45	16.31	OC H3.4 Chondrule	bkr1dp012
		1.92	1.51-2.39	8.41		
186	Celuta	1.02	0.77-1.19	5.83	CC CV3 CAI	c1tm06
189	Phthia	0.92	0.75-1.44	15.04	No Corresp.	-
		1.98	1.57-2.19	5.94		
192	Nausikaa	0.99	0.75-1.55	12.52	No Corresp.	-
		1.97	1.57-2.46	5.29		
198	Ampella	0.90	0.77-1.51	11.70	OC H5	latb85
		1.81	1.49-2.11	6.71		
207	Hedda	0.76	0.60-0.89	1.25	No Corresp.	-
230	Athamantis	0.88	-	-	Olivine Met. †	bkr1dd121
234	Barbara	0.84	0.75-0.93	3.10	CC CV3 (6)	-
		2.10	1.59-2.44	4.58		
248	Lameia	-	-	-	EC E4 Heated †	cdmt40
261	Prymno	0.92	0.83-1.09	1.98	No Corresp.	-
298	Baptistina	1.03	0.75-1.56	5.60	OC LL4	c1oc02b
		2.00	1.58-2.29	3.90		
302	Clarissa	-	-	-	CC CM Unusual	ncmb18
313	Chaldaea	0.71	0.57-0.85	2.21	CC CM2	mgp096
326	Tamara	0.67	0.55-0.86	2.71	CC CM2	ccms01
329	Svea	-	-	-	CC CM2 (5)	-
336	Lacadiera	-	-	-	CC CM2 heated	cdmb64
337	Devosa	0.90	0.74-1.10	2.71	Mesosiderites (8)	-
345	Tercidina	0.69	0.54-0.88	2.49	No Corresp.	-
376	Geometria	0.95	0.74-1.51	20.28	OC L6 Irradiated	c1oc11d35
		1.80	1.56-2.14	2.40		
435	Ella	-	-	-	EC E4 Heated	cgmt40
474	Prudentia	-	-	-	No Corresp.	-
495	Eulalia	-	-	-	CC CV3	mgp130
556	Phyllis	0.92	0.74-1.48	8.17	OC H3.8	c1tb91
		1.83	1.53-2.27	6.21		
623	Chimaera	0.72	0.58-0.84	1.25	CC	bkr1mt02510
654	Zelinda	0.67	0.52-0.84	2.64	CC CM2 (5)	-
732	Tjilaki	-	-	-	No Corresp.	-
752	Sulamitis	0.71	0.58-0.90	1.96	CC CM2	cgp098
914	Palisana	0.69	0.52-0.86	4.28	CC CM2	c2mb64

**Notes.** (1): Kelley & Gaffey (2000), (2): Barucci et al. (2008), (3): Reynolds et al. (2009), (4): Avdellidou et al. (submitted), (5): Fornasier et al. (2014), (6): Devogèle et al. (2018), (7): Clark et al. (2009), (8): Vernazza et al. (2009). OC: Ordinary Chondrites; CC : Carbonaceous Chondrites; EC: Enstatite Chondrites. Objects with a † symbol indicate asteroids having only the visible part of the spectra.